

Research Article

HYPEREION—A precision system for the detection of the absorption profile centred at 78 MHz in the radio background spectrum

N. Patra , R. Wayth, M. Sokolowski, D. Price, B. McKinley and D. Kenney

International Centre for Radio Astronomy Research, Curtin University, Bentley, WA 6102, Australia

Abstract

The report of a detection of an absorption profile centred at 78 MHz in the continuum radio background spectrum by the EDGES experiment and its interpretation as the redshifted 21 cm signal of cosmological origin has become one of the most debated results of observational cosmology in recent times. The cosmological 21 cm has long been proposed to be a powerful probe for observing the early Universe and tracing its evolution over cosmic time. Even though the science case is well established, measurement challenges posed on the technical ground are not fully understood to the level of claiming a successful detection. EDGES's detection has naturally motivated a number of experimental attempts worldwide to corroborate the findings. In this paper, we present a precision cross-correlation spectrometer HYPEREION purpose-designed for a precision radio background measurement between 50–120 MHz to detect the absorption profile reported by the EDGES experiment. HYPEREION implements a pre-correlation signal processing technique that self-calibrates any spurious additive contamination from within the system and delivers a differential measurement of the sky spectrum and a reference thermal load internal to the system. This ensures an unambiguous 'zero-point' of absolute calibration of the purported absorption profile. We present the system design, measurement equations of the ideal system, systematic effects in the real system, and finally, an assessment of the real system output for the detection of the absorption profile at 78 MHz in the continuum radio background spectrum.

Keywords: 21 cm Global signal – Observational cosmology – 21 cm cosmology – cosmic radio background – radio background measurements – astronomical instrumentation: radio telescopes – astronomical techniques: Principal Component Analysis

(Received 17 August 2022; revised 21 February 2023; accepted 19 April 2023)

1. Introduction

The first billion years of Cosmic history have remained a mystery to date due to the complete unavailability of any direct observable since the Cosmic Microwave Background (CMB). An incisive probe to this era is the cosmological 21 cm signal—the atomic line radiation from the primordial neutral hydrogen (HI, rest wavelength ~ 21 cm). Prior to the formation of any astronomical sources of radiation, the primordial neutral hydrogen-filled the Universe homogeneously and isotropically and, in interaction with the CMB, resulted in HI line radiation. Therefore, the brightness temperature of this all-sky line radiation at any epoch is a testimony to the ongoing astrophysical processes that led to the formation of the first astronomical sources of radiation (Furlanetto 2006). Accelerated expansion of the Universe redshifted the 21 cm line to lower frequencies given by $\nu = \frac{\nu_0}{(1+z)}$ where 'z' is the cosmological redshift and ν_0 is the rest frame frequency of the 21 cm signal. Therefore, tracking this line over cosmological redshifts, i.e., cosmic time, can provide unparalleled information on how the Universe evolved from a homogeneous and isotropic state to the sources of first light. Different astrophysical processes affected the line strength over redshifts, making it visible either in emission or in absorption against the CMB.

Evolution of the 21 cm line over cosmic time has chronologically marked various epochs in cosmic time known as the Dark Ages (DA), the Cosmic Dawn (CD) and the Epoch of Reionisation (EoR); for an overview, see Furlanetto, Oh, & Briggs (2006), Morales & Wyithe (2010), Pritchard & Loeb (2012). A theoretical prediction of T_{21} at various 'z' is shown in Figure 1.

The redshifted 21 cm line, however, constitutes a minuscule fraction of the total background radiation below 200 MHz. More recent history of galactic and extragalactic radiation collectively constitute the bulk of the continuum radio background at these frequencies (Patra et al. 2015; Mozdzen et al. 2019) which is 10^5 times stronger than the 21 cm signal. Therefore, detection of the redshifted 21 cm signal requires a precision measurement of continuum radio background spectrum with an accuracy of $1:10^5$ or higher over a wide frequency (Shaver et al. 1999). At low radio frequencies requiring electrically large radio telescopes with large fractional errors of measurements, this poses a mammoth engineering challenge to achieve a successful detection of the 21 cm signal. Furthermore, the continuum radio background below 200 MHz is, at best, poorly studied, with no prior knowledge of its frequency structures.

A number of experiments have commenced worldwide in the past ten years (see Table 1), each with unique complexity in system design, calibration and analysis formalism. Of these, only three (EDGES, SARAS, & LEDA) have produced science-grade data (Bowman et al., 2018; Singh et al., 2018; Bernardi et al., 2016) and constrains on the cosmological 21 cm signal. In 2018, the EDGES experiment reported the detection of an absorption profile in their

Corresponding author: N. Patra, Email: nipanjana.patra@prelectdevices.com.

Cite this article: Patra N, Wayth R, Sokolowski M, Price D, McKinley B and Kenney D. (2023) HYPEREION—A precision system for the detection of the absorption profile centred at 78 MHz in the radio background spectrum. *Publications of the Astronomical Society of Australia* 40, e026, 1–21. <https://doi.org/10.1017/pasa.2023.25>

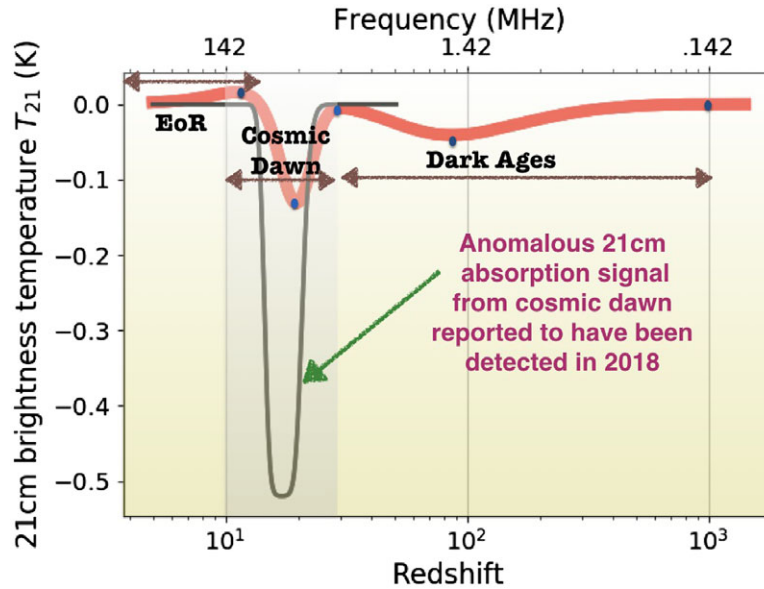


Figure 1. A representative model of the redshifted 21 cm signal/Hi line as a differential brightness temperature relative to the CMB over cosmological redshifts (Cosmic time). The CMB forms at the extreme right at $z \approx 1100$, $z = 0$ is time today at the extreme left. Following the CMB, the homogeneous and isotropic Universe evolved through the Dark Ages (DA) $\approx z > 35$, leading to the formation of the first sources of light during the Cosmic Dawn (CD) $35 > z > 15$. Throughout the DA and the CD, the 21 cm signal is expected to be visible in absorption against the CMB. As these sources further evolved, they ionised the remaining neutral hydrogen in their surrounding - an era known as the Epoch of Reionisation (EoR) when the 21 cm signal is expected to be seen in emission against the CMB. The top scale shows the redshifted frequencies at which the line is visible at each redshift. The primary quantity of interest is the redshifts and amplitude of the 21 cm signal at the minimum/maximum line brightness temperatures.

radio background measurements centred at 78 MHz corresponding to a redshift $z = 18$ over a bandwidth of 19 MHz (Bowman et al. 2018). When modelled as a flattened Gaussian of the form,

$$T_{21} = -A \frac{(1 - e^{-\tau e^{-B}})}{(1 - e^{-\tau})} \quad (1)$$

where,

$$B = \frac{4(v - v_0)^2}{w^2} \log \left[-\frac{1}{\tau} \log \left[\frac{(1 + e^\tau)}{2} \right] \right] \quad (2)$$

A is the amplitude of the absorption trough measured at the centre frequency ν_0 , w is the full-width at half-maximum, and τ is the flattening factor of the Gaussian. The best-fit value of amplitude A of the absorption profile is reported to be $500^{+0.5}_{-0.2}$ mK, the centre frequency $\nu_0 = 78 \pm 1$ MHz, and the full-width half maximum is $w = 19^{+4}_{-2}$ MHz. This detection has led to multiple plausible explanations, both as cosmological 21 cm signal. Barkana (2018), Fialkov, Barkana, & Cohen (2018), Barkana et al. (2018), Xiao et al. (2019), as well as unaccounted instrumental artefacts (Hills et al. 2018; Singh & Subrahmanyan 2019; Sims & Pober 2020; Bevins et al. 2021). When interpreted as the 21 cm signal from the Cosmic Dawn, the amplitude of the absorption profile is a factor of two larger than the largest amplitude theoretically predicted. The standard cosmological models of the evolution of the Universe can not explain this result. It is also incompatible with current astrophysical predictions of the 21 cm signal from the knowledge of the high-redshift galaxies, their characteristics and population densities. Therefore, it warrants an extension of the standard cosmological and particle physics models to explain the observed detection in the cosmological context. In an independent effort, SARAS-3 experiment (Singh et al. 2021) have reported the absence of the said absorption trough in their measurements. SARAS-3 is

located in the northern whereas EDGES is located in the southern hemisphere. For extragalactic isotropic radio background, such differences are inconsequential. However, local galactic structures and multipath effects in the observation environment can be of consequence along with non-optimal calibration of instrument response. Therefore the need for independent verification is pressing.

The ongoing Global 21 cm experiments for 21 cm signal detection are all composed of wideband antennas connected with a correlation spectrometer. They differ in antenna frequency response and strategy for in-depth calibration of the systematic instrumental effects. Earlier attempts at radio background measurements largely depended on the software calibration of instrument response by parametric modelling. However, they ran the risk of losing the cosmological 21 cm signal in the process of instrument calibration. HYPEREION implements manifold improvements in instrument design, measurement method, calibration strategy, and data interpretation over first-generation experiments and has a narrowed target of detecting only one plausible absorption profile predetermined by the EDGES detection. This improves the precision of instrument characterisation.

This paper presents the instrument design that evolved with the prime focus of detecting the aforesaid absorption profile. Section 2 describes the telescope system, including antenna, analogue, digital receivers and their constituents. Section 3 describes the measurement equations and calibration for ideal system performance. Deviation from the ideal system performance and its effects on the measurement equations and the final measured spectra are described in detail in section 4. Section 5 describes the data, and section 6 assesses the spectral properties of the instrument when the antenna input is terminated with a precision 50 Ohm load with a perfect impedance match, an open load with a perfect mismatch.

Table 1. Experiments seeking to measure the 21-cm all-sky signal.

Experiment	Reference	Status
Experiment to Detect the Global EoR Signal	Rogers & Bowman (2008)	ongoing
Experiment to Detect the Global EoR Signal, low-band	Bowman et al. (2018)	ongoing
Large-aperture Experiment to detect the Dark Ages	Price et al. (2018)	ongoing
Broadband Instrument for Global HydrOgen ReioNisation Signal	Sokolowski et al. (2015)	concluded
Shaped Antenna measurement of the background RAdio Spectrum	Patra et al. (2013)	concluded
Shaped Antenna measurement of the background RAdio Spectrum	Singh et al. (2018)	concluded
Shaped Antenna measurement of the background RAdio Spectrum	Nambissan T. et al. (2021)	ongoing
Sonda Cosmológica de las Islas para la Detección de Hidrógeno Neutro	Voytek et al. (2014)	concluded
Probing Radio Intensity at high-z from Marion	Philip et al. (2019)	ongoing
Long Wavelength Array at Sevilleta, beamformer	Dilullo, Taylor, & Dowell (2020)	ongoing
Short spacing Interf Telescope probing cosmic dAwn and epoch of ReionisAtion	Thekkepattu et al. (2022)	in development
Radio Experiment for the Analysis of Cosmic Hydrogen	de Lera Acedo (2019)	in development
Mapper of the IGM Spin Temperature	Bye (2021)	in development
Dark Ages Radio Explorer	Burns et al. (2017)	proposed
Dark Ages Polarimetry Pathfinder	Burns et al. (2021)	proposed

Finally, the final spectrum and the instrument's ability to detect the cosmological 21 cm signal are discussed in section 6.

2. System description

HYPEREION is a single-element radio telescope system with a two-channel interferometric/cross-correlation spectrometer. The system architecture is directly motivated by the SARAS system design (Patra et al. 2013), but several changes are implemented. Firstly, the operating range of SARAS was 87.5–175 MHz. HYPEREION is designed to be operated between 50–120 MHz. The antenna element is redesigned following the SARAS antenna design for use in this frequency range. The second and most significant difference from the SARAS architecture is the introduction of a low-noise amplifier right after the directional coupler in HYPEREION. This was implemented to ensure that system noise radiated by the HYPEREION antenna is kept below the Murchison Radio Observatory's recommended emission level. This alters the HYPEREION measurement equation from that of SARAS. HYPEREION measures the continuum sky spectrum on top of a 400 K amplifier noise coupled directly into the antenna signal path. In SARAS, the amplifiers contributed to the measurement only due to the cross-coupling and that too at a level of 1.5–2 K. The antenna signal is split into two halves early on and fed into two identical analogue receiver chains that bandlimit the signal between 30–120 MHz, and amplify them. Notable here, the lower cut-off frequency for the system design is chosen to be 30 MHz, which is below the lower cut-off frequency of observation 50 MHz. This ensures that the instrumental edge effects are beyond the observation band. Two receiver output voltages are sampled, digitised and Fast Fourier Transformed. Data in corresponding frequency channels are multiplied to compute the cross-power spectrum. A broadband calibration noise is injected into the system prior to splitting the antenna signal. Each receiver also contributes its own noise to the signal path. However, since the receiver noises are independent, they are uncorrelated. Therefore, ideally, the receiver noise contribution in the computed cross-power spectrum is zero. This is the primary motivation

for adopting an interferometric receiver (Figure 2). Splitting the antenna signal into two by a power splitter enables incorporating a form of mechanical phase switching. As a result, any spurious additive response added in the signal paths after the switching is cancelled in the difference spectrum. This is described in detail in the measurement equation section.

2.1. Antenna

The antenna element is the most critical component of single-element telescopes for global 21 cm signal detection. Unfortunately, the antenna response can not be calibrated for an all-sky measurement using an external calibrator on the sky. The antenna response affects the sky signal received at the antenna output in two ways. Firstly, the antenna beam $G(\theta, \nu)$ is a function of frequency ν , and θ is the angle measured from the dipole axis (length of the dipole). As a result, the antenna may receive signals from a larger part of the sky at some frequencies than others. Secondly, the antenna's coupling efficiency at any frequency depends on the Ohmic losses within the antenna and the impedance mismatch between the antenna and the transmission line, represented by antenna voltage reflection coefficient $\Gamma_a(\nu)$.

Ideally, to preserve the spectral characteristics of the 21 cm global signal, the antenna should be frequency-independent, i.e., $G_a(\theta, \nu) = G_a(\theta)$ and $\Gamma_a(\nu) = \text{constant}$ over the observing band. However, the theoretical predictions of the global 21 cm signal are expected to be spread over a wide frequency range between 30–200 MHz. At these low frequencies, the physical size of the antenna is large. Owing to the large manufacturing tolerances at low frequencies, the frequency-independent performance of the antenna over multiple octaves is compromised. As a result, the antenna frequency response can generate spectral features that can be confused with the global 21 cm signal. In the absence of a true frequency-independent antenna at low frequencies, ongoing global 21 cm experiments use a variety of electrically short antenna structures that have smooth spectral responses over the desired frequency range. In this case, G_a, Γ_a is described

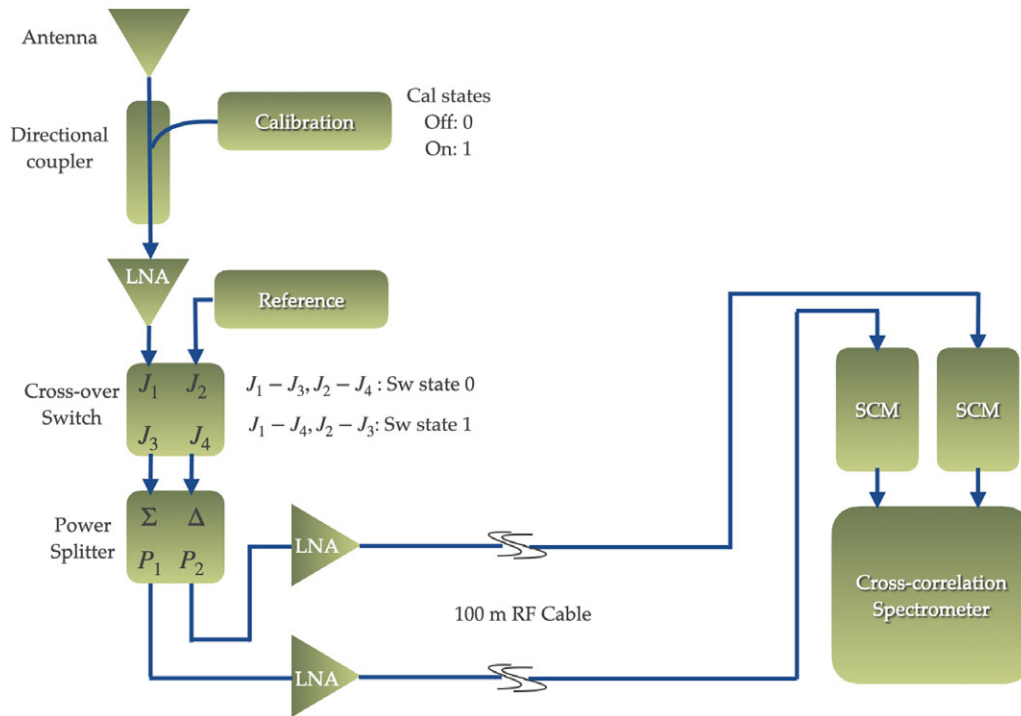


Figure 2. Schematic diagram of the HYPEREION system. The antenna and the calibration noise are fed into the direct and the coupled port of a directional coupler and fed to the first stage of LNA. The output of the LNA and a reference noise is alternately connected to the Σ and the Δ port of a power splitter. The power splitter outputs are fed into two second-stage LNAs, outputs of which are transported by a pair of RF cables 100 m away from the antenna and fed into the Signal Conditioning Modules (SCM). The SCM further amplifies and bandlimits the signal between 30–120 MHz before feeding it into the Cross-correlation Spectrometer. The Spectrometer samples, digitises the signal, and computes a Fast Fourier Transform to yield the power spectrum.

with a polynomial of low order in frequencies as described in Mahesh et al. (2021), Raghunathan, Shankar, & Subrahmanyam (2013).

For HYPEREION, we adopt a variant of the electrically short fat dipole (Raghunathan et al. 2013) to operate between 30–120 MHz (Figure 4). It is a three-dimensional structure made of Aluminium which is symmetric around the dipole axis (z -axis) with a square cross-section in the x - y plane. The key design parameter responsible for the wideband performance of this antenna is its surface profile. Raghunathan et al. (2013) had shown that a smooth frequency response over an octave bandwidth is achieved between 87.5–175 MHz by shaping the edge of each surface as $x = x_0 + A \sin^\alpha \left(\frac{2\pi z}{\lambda} \right)$ (Figure 4) where x is the half diagonals of the square cross sections on the x - y plane. Therefore, we tune the parameters x_0 , A , and α to design the antenna between 30–120 MHz (Figure 3). Figure 7 shows the measurements of antenna return loss $S_{11}(\nu)$ as a function of frequencies. Details of antenna simulation and measurements are out of this paper's scope and will be discussed elsewhere.

2.2. Analogue receiver

HYPEREION analogue receiver is implemented in two modules. The frontend module is located in the field at the antenna base. The backend module is located 100 m away from the antenna in an electromagnetically shielded enclosure known as the Telstra-Hut that provides 80 dB attenuation to the RFI generated inside the hut. The separation ensures the radio frequency interference (RFI) generated in the digital system, also located in Telstra-Hut, is not

coupled into the system via the antenna. The frontend box receives the antenna output and adds a broadband calibration noise into the signal path by a directional coupler. The output of the directional coupler is fed into a low-noise amplifier. The output of the amplifier is fed into the Σ (sum) port of a four-port power splitter via a mechanical switch. A precision 50 Ohm termination is connected to the Δ (difference) port of the power splitter via the mechanical switch. The mechanical switch alternates the antenna and the reference noise between the Σ and the Δ port. Outputs of the power splitter are fed into a pair of identical low-noise amplifiers (LNAs). Each of these RF components is so chosen that any uncalibrated spectral feature introduced in the final bandpass calibrated spectrum does not affect the detectability of the Global signal.

- **Directional coupler:** A coaxial directional coupler (Figure 6) is used in reverse to couple a broadband calibration noise in the antenna path. The antenna is connected to port P_2 of the directional coupler by an RF cable of length L . The calibration noise is connected to the coupled port P_3 of the directional coupler. The calibration noise is turned on-off every 0.5 s. The antenna and the calibration noise travel downstream via port P_1 and follow the identical signal path, including the multipath reflections. Therefore, the calibration noise is able to completely calibrate the complex system bandpass response to antenna noise from this point onwards. From hereon, port P_1 is referred to as our calibration plane. Any spurious spectral response imprinted on the antenna

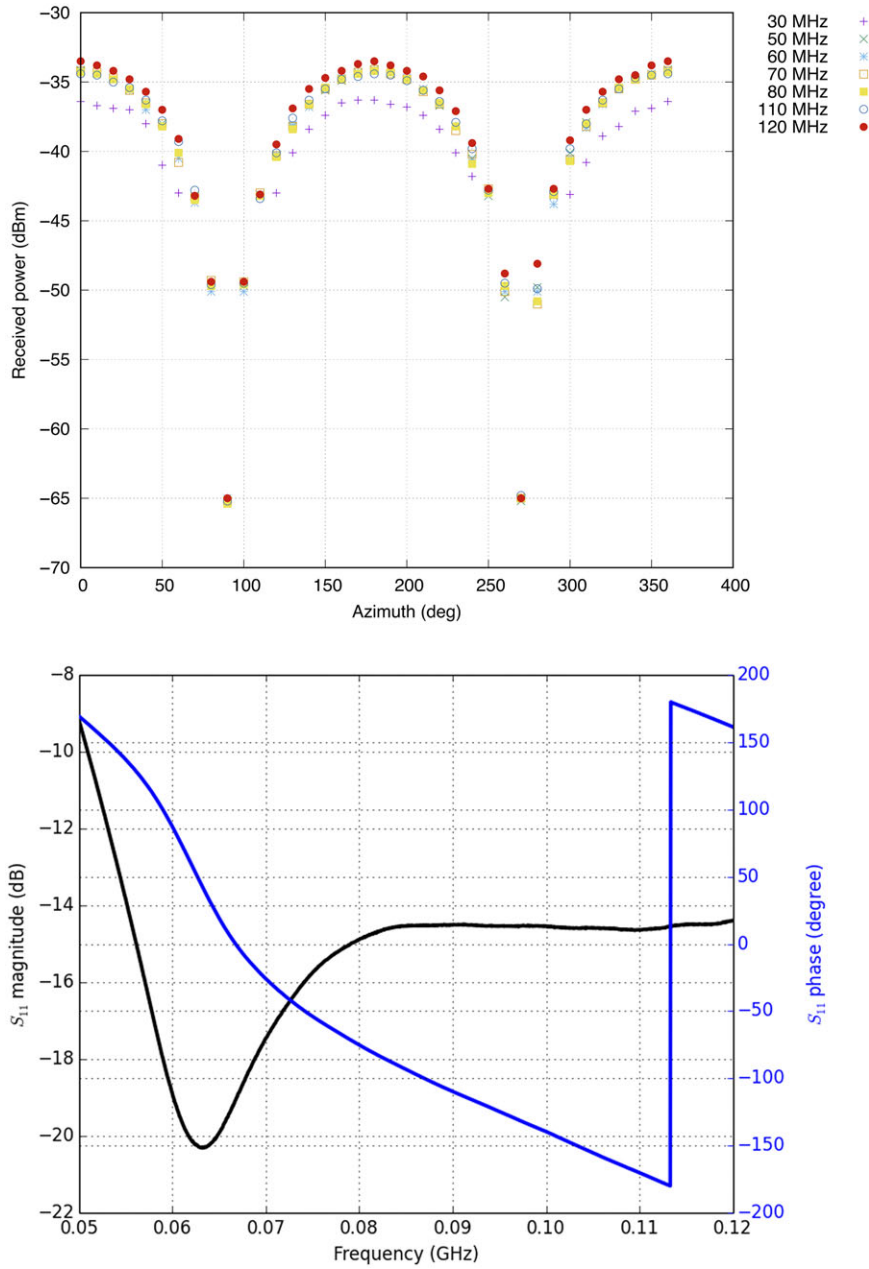


Figure 3. Panel 1: Antenna beam pattern measured between 30–120 MHz. The measured beam patterns overlap at all measurement frequencies up to 50 MHz. Towards the lowest end of the band at 30 MHz, the antenna gain reduces at all position angles. This is why the lower cut-off for observation is kept at 50 MHz while the antenna is designed with a lower cut-off at 30 MHz. Panel 2: Magnitude and phase of the measured antenna return loss S_{11} .

signal prior to reaching port P_1 of the directional coupler remains in the bandpass calibrated spectrum.

- **Low-Noise Amplifier 1:** The directional coupler output is fed to a low-noise-amplifier+attenuator assembly, referred to as stage1-LNA from hereafter. The amplifier noise figure is typically 3.8 dB between 10–500 MHz, equivalent to a receiver noise temperature of 400 K. We chose an amplifier with a relatively higher noise figure as it has a better input match than a very low-noise amplifier. It is the input match of the first stage of the amplifier that critically determines the spectral smoothness of the

calibrated data as shown in the measurement equation. For this amplifier, the receiver noise becomes comparable to that of the sky at the upper end of the band at 120 MHz. However, for the purpose of corroboration of the reported Cosmic Dawn signal that extends up to 82 MHz, this amplifier is indeed the best choice. This assembly aims to prevent any signal originating from the rest of the receiver downstream from propagating upward to the antenna and radiating in the environment. Components such as the RF mechanical switch is periodically energised and de-energised. The contact stabilisation time of the

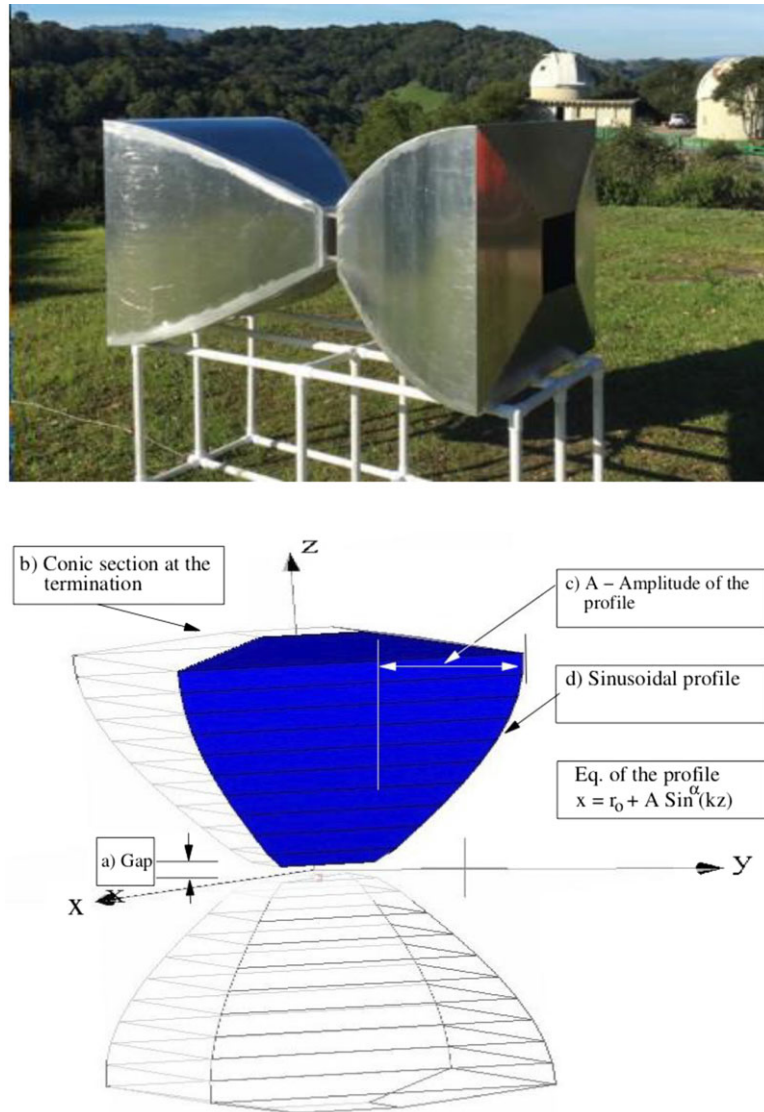


Figure 4. Panel 1: The HYPEREION antenna is a fat dipole antenna that is electrically short between 30–120 MHz. The basic design is adopted from Raghunathan *et al.* (2013). Bottom: Schematic reproduced from Raghunathan *et al.* (2013) showing various design parameters. We tune these design parameters to obtain the optimum antenna performance between 30–120 MHz to achieve a spectral response that is non-degenerate with the Cosmic Dawn signal of the form Equation (1). The resulting antenna beam pattern $G(\theta, \nu)$ and magnitude and phase of the return loss $\Gamma_r(\nu)$ is shown in Figure 3.

switch is about 20 ms, during which a transient burst of energy is coupled to the main signal path that propagates upstream towards the antenna and radiates. The digital receiver system that is clocked over a range of rates can generate transient broadband radiation that can couple to the main signal path, propagate upstream to the antenna and radiate. While we exclude the 20 ms data during every transition to remain unaffected by this, other experiments located at the same observatory might be sensitive enough to pick up these transient broadband radiations. Any upward travelling signal is first attenuated by 20 dB first by the attenuator and then by an additional 22 dB by the reverse isolation of the LNA. Based on the mil-standard test *MIL – STD461F* performed in an EMC chamber, this provides sufficient isolation of any upward

travelling noise from being radiated into the surroundings at the Murchison Radio Observatory.

- **Mechanical Switch:** Output of the stage1-LNA is connected to a two-input/two-output mechanical RF transfer switch (Figure 5). When the switch is de-energised, referred to state-‘0’ hereon, J_1 internally connects to J_3 , and J_4 internally connects to J_2 . In this switch state, antenna (+calibration) noise incident to port J_1 is transferred to the ‘sum’ (Σ) port of a power splitter. A precision 50 Ohm load, termed as the ‘reference’ load from hereon, is externally connected at port J_4 of the switch. Noise from the reference incident to port J_4 is transferred to the ‘difference’ (Δ) port of the same power splitter. When the switch is energised, referred to as state ‘1’ hereon, J_1 internally connects to J_2 , and J_4 internally connects to J_3 . The antenna

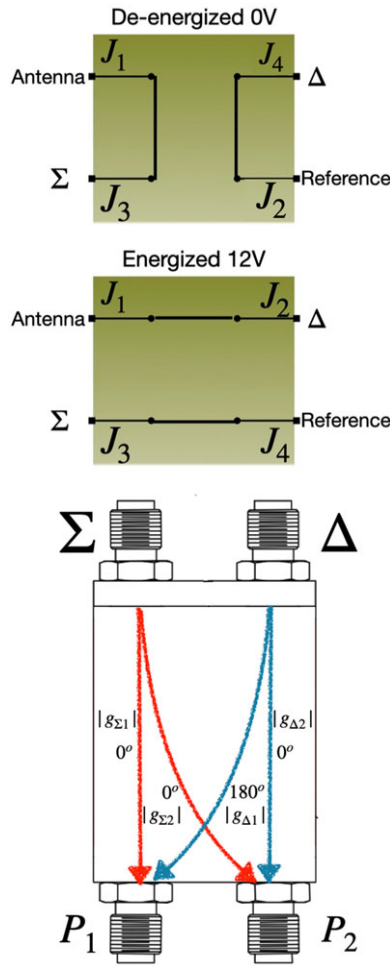


Figure 5. Top: Schematic diagram of the switch. In the de-energised state of the switch port J_1 is electrically connected to J_3 and J_2 is connected to J_4 . In this state, the antenna is connected to the Σ port of the power splitter, and the reference is connected to the Δ port. In the energised state, J_1 is electrically connected to J_2 and J_3 is connected to J_4 . In this state, the antenna is connected to the Δ port of the power splitter, and the reference is connected to the Σ port. Bottom: Schematic diagram of a power splitter: Any noise connected to the Σ port of the splitter is split into two halves ‘in-phase’. Any noise connected to the Δ port of the splitter is split into two halves ‘out of phase’.

(+calibration) noise is now transferred to the (Δ) port of the splitter, and the reference noise is transferred to the (Σ) port. It takes 20 ms for the RF mechanical switch to establish the electrical contact after a state transition. This sets the lowest integration time to be >20 ms. The insertion-loss between port $J_1 - J_3$, $J_4 - J_2$, $J_1 - J_2$, $J_4 - J_3$ are 0.01 dB between 10–200 MHz. In state ‘0’, isolation between port $J_1 - J_2$, and $J_4 - J_3$ is >90 dB. In state ‘1’, isolation between port $J_1 - J_3$, and $J_4 - J_2$ is also >90 dB. Therefore, antenna (+calibration) and reference noise follow isolated paths with no mutual coupling within the switch. As a consequence, the calibration noise is unable to calibrate the bandpass response of the switch imprinted on the reference noise.

The switch cycles through state ‘0’, and ‘1’ every 1 s and alternately connects the antenna and the reference noise to Σ and Δ port of the power splitter. In each position of the switch, the calibration noise is turned on and off for 0.5 s.

- Power Splitter:** The output ports J_3 , and J_2 of the switch are connected to the Σ and the Δ port of the power splitter. The complex voltage gains within the power splitter are denoted as $g_{\Sigma 1}, g_{\Sigma 2}, g_{\Delta 1}, g_{\Delta 2}$ (Figure 5). $|g_{\Sigma 1}|^2 = |g_{\Sigma 2}|^2 = |g_{\Delta 1}|^2 = |g_{\Delta 2}|^2 = -3$ dB, $\angle g_{\Sigma 1} - \angle g_{\Sigma 2} = 0^\circ$, i.e., any signal entering the Σ port of the splitter is split into two parts with equal amplitude and in-phase. $\angle g_{\Delta 1} - \angle g_{\Delta 2} = 180^\circ$, i.e., any signal entering the Δ port of the splitter is split into two parts with equal amplitude and out of phase. The reference is an additive blackbody noise at ambient temperature. Downstream from P_1, P_2 , the antenna, the calibration, and the reference noise follow the identical signal path. Therefore, the calibration noise fully calibrates any system bandpass response to these noises from this point onwards.
- Low noise amplifier 2,3** The power splitter outputs are directly connected to two identical Low-Noise Amplifiers that amplify the input signals by 22 dB. Amplifier outputs are sent downstream about 100 m away to the Telstra-Hut into the backend receivers module, which houses two identical two-stage filter-amplifier chains. It band limits the signal between 30–120 MHz and further amplifies it before feeding it to the digital cross-correlator. Since the two receiver noises are independent, they are uncorrelated. Therefore, the contribution of these two amplifiers to the cross-power output is ideally zero. Secondly, the mechanical switch and the power splitter assembly enable cancelling any spurious correlated noise that is added downstream to both channels after the switching state, such as the broadband correlator noise generated within the digital correlator. The digital correlators are clocked at a range of rates. Such clock signals generate broadband emissions to both analogue signal paths generates spurious correlation at the final digital correlator outputs. Alternating the position of the antenna and the reference between the sum and the delta port of the power splitter cancels such spurious additive contribution, as shown in section 3.

2.3. Digital receiver

Output voltages from the analogue backend module are fed into a digital data processing unit where these voltages are sampled and digitised by a SIGNATEC PX-1500—a two-channel 8 bit digitiser board at a sampling rate of 300 MHz. The digitised output is fed into a GPU that computes the Fourier Transform of each receiver channel voltage by an 8 192-point Fast Fourier Transform (FFT) algorithm. The complex voltages at corresponding frequencies between two channels are then multiplied to compute the cross-power spectrum across the observing band. The auto-correlation spectra of individual channels are also computed. The digital spectrometer can compute one cross-power spectrum every 13 ms. However, the switching speed of the mechanical switch determines the shortest integration time. Therefore, one spectrum is recorded every 20 ms. The broadband RFI generated within the digital system is contained within the Telstra Hut as per the mil standard requirement of the Murchison Radio Observatory. The RF switching cancels any additive noise electronically generated within the digital system during computation.

Table 2. HYPEREION observing cycle. The four rows show the switch positions and on (1) and off (0) states of the calibration noise through which the system cycles during the observations.

State name	Switch state	CAL state
OBS0	0	0
CAL0	0	1
OBS1	1	0
CAL1	1	1

3. Measurement equations for ideal system

During observation, HYPEREION cycles through four different states as described in Table 2. When de-energised, i.e., in switch state '0', the antenna and the reference are connected to the Σ , Δ port, respectively. In this state, when the calibration noise is 'off', i.e., CAL state '0', the measured spectrum is contributed by the antenna and the reference noise and denoted as OBS0. In the same switch state, when the calibration noise is turned 'on', i.e., the CAL state is '1', the measured spectrum is denoted as CAL0. The calibration noise is turned on and off once again when the switch changes its state to '1', i.e., connects the antenna and reference to Δ , Σ ports, respectively. The corresponding spectra are marked as OBS1, CAL1. We derive the measurement equations for each state assuming ideal system performance. The three key assumptions for an ideal system are,

- In an ideal system, each RF component is perfectly matched with any other component/transmission line connected to it. As a result, there is no internal reflection of any noise voltages that can result in multipath propagation effects.
- When the signal is split by the power splitter, the path gains $|g_{\Sigma 1}|^2 = |g_{\Sigma 2}|^2 = |g_{\Delta 1}|^2 = |g_{\Delta 2}|^2 = |g|^2 = -3$ dB, $\angle g_{\Sigma 1} - \angle g_{\Sigma 2} = 0^\circ$ and $\angle g_{\Delta 1} - \angle g_{\Delta 2} = 180^\circ$.
- In an ideal system, the receiver noises propagated only downstream.

We denote the antenna and the calibration temperature at the mainline output (port P_2 of the directional coupler) as T_a , T_{cal} , the reference noise temperature as T_{ref} and the noise temperature of the stage1-LNA as T_{lna} .

We denote the antenna noise voltage at the output of the directional coupler as v_a , the total gain of the stage1-LNA assembly as G and from the output of the power splitter up to the input of the spectrometer along channel 1, 2 as G_1 , G_2 . The frequency dependence of these terms is implicit.

3.1. Ideal system response to antenna noise

At system state OBS0, i.e., when the antenna is connected to the Σ port of the splitter, the antenna voltages at the input of the correlator are,

$$v_{a1} = gGG_1v_a \quad (3)$$

$$v_{a2} = gGG_2v_a \quad (4)$$

The cross-power at the output of the spectrometer due to antenna noise,

$$\begin{aligned} P_{oa} &= v_{a1}v_{a2}^* \\ &= |g|^2|G|^2G_1G_2^*P_a \end{aligned} \quad (5)$$

Similarly, at system state OBS1, i.e., when the antenna is connected to the Δ port of the splitter, the antenna voltages at the input of the correlator are,

$$v_{a1} = gGv_aG_1 \quad (6)$$

$$v_{a2} = -gGv_aG_2 \quad (7)$$

The cross-power at the output of the spectrometer due to antenna noise,

$$\begin{aligned} P_{1a} &= v_{a1}v_{a2}^* \\ &= -|g|^2|G|^2G_1G_2^*P_a \end{aligned} \quad (8)$$

The phase imbalance of 180° between the voltages along the two arms, when the antenna noise is connected at the Δ port, is reflected in the negative voltage alone in one arm.

3.2. Ideal system response to receiver noise

Receiver noise in the HYPEREION is contributed by the first low-noise-amplifier alone. The noise figure of the low-noise amplifier (number) is 3.8 across our frequency band. Therefore, a mean receiver noise ranging 400 K is added to the antenna noise at the output of the LNA. We denote the LNA noise voltage referred to its input as v_{lna} . Just like the antenna, at system state OBS0, the LNA1 is connected to the Σ port of the splitter. Receiver voltages at the input of the correlator are,

$$v_{rec1} = gGv_{lna}G_1 \quad (9)$$

$$v_{rec2} = gGv_{lna}G_2 \quad (10)$$

The cross-power at the output of the spectrometer due to receiver noise,

$$\begin{aligned} P_{or} &= v_{rec1}v_{rec2}^* \\ &= |g|^2|G|^2G_1G_2^*P_{lna} \end{aligned} \quad (11)$$

In system state OBS1, the LNA1 is connected to the Δ port of the splitter. Receiver voltages at the input of the correlator are,

$$v_{rec1} = gGv_{lna}G_1 \quad (12)$$

$$v_{rec2} = -gGv_{lna}G_2 \quad (13)$$

The cross-power at the output of the spectrometer due to receiver noise,

$$\begin{aligned} P_{1r} &= v_{rec1}v_{rec2}^* \\ &= -|g|^2|G|^2G_1G_2^*P_{lna} \end{aligned} \quad (14)$$

3.3. Ideal system response to reference noise

At system state OBS0, the reference is connected to the Δ port of the splitter. The reference voltages at the input of the correlator are,

$$v_{ref1} = gv_{ref}G_1 \quad (15)$$

$$v_{ref2} = -gv_{ref}G_2 \quad (16)$$

The cross-power at the output of the spectrometer due to reference noise,

$$P_{oref} = v_{ref1} v_{ref2}^* = -|g|^2 G_1 G_2^* P_{ref} \tag{17}$$

At system state OBS1, the reference is connected to the Σ port of the splitter. The reference voltages at the input of the correlator are,

$$v_{ref1} = g v_{ref} G_1 \tag{18}$$

$$v_{ref2} = g v_{ref} G_2 \tag{19}$$

The cross-power at the output of the spectrometer due to reference noise,

$$P_{1ref} = v_{ref1} v_{ref2}^* = |g|^2 G_1 G_2^* P_{ref} \tag{20}$$

3.4. Ideal system response to total noise

The total complex cross-power spectrum measured in OBS0 state

$$P_{OBS0} = P_{oa} + P_{or} + P_{oref} + P_{cor} = |g|^2 |G|^2 G_1 G_2^* \left(P_a + P_{lna} - \frac{P_{ref}}{|G|^2} \right) + P_{cor} \tag{21}$$

Since the calibration noise is injected into the antenna path at the output of the directional coupler, when the calibration noise is ‘on’, the total cross-power output in state CAL0 is,

$$P_{CAL0} = |g|^2 |G|^2 G_1 G_2^* \left(P_a + P_{cal} + P_{lna} - \frac{P_{ref}}{|G|^2} \right) + P_{cor} \tag{22}$$

P_{cor} represents any additive noise that is either coupled to both signal chains after the switch and results in correlated output power or any noise generated within the digital system during computation that is added to the computed cross power. Since it is added after the switching state, P_{cor} doesn’t change sign with the switch position. The reference noise is injected into the system after the injection of the calibration noise. The term $\frac{P_{ref}}{|G|^2}$ indicates the reference noise contribution referred to the input of the LNA1 assembly.

Similarly, when the antenna and the reference positions are switched, the total complex cross-power spectrum measured in OBS1, CAL1 state are,

$$P_{OBS1} = -|g|^2 |G|^2 G_1 G_2^* \left(P_a + P_{lna} - \frac{P_{ref}}{|G|^2} \right) + P_{cor} \tag{23}$$

$$P_{CAL1} = -|g|^2 |G|^2 G_1 G_2^* \left(P_a + P_{cal} + P_{lna} - \frac{P_{ref}}{|G|^2} \right) + P_{cor} \tag{24}$$

3.5. Cancellation of spurious additive response

Equations (21), (22), (23), (24) are the four successive spectra measured by the spectrometer over a period of two seconds. From these, the bandpass calibrated spectra are derived. Differencing Equations (21), (23) cancels the unwanted additive contribution P_{cor} .

$$P_{OBS} = \frac{P_{OBS0} - P_{OBS1}}{2} = |g|^2 |G|^2 G_1 G_2^* \left(P_a + P_{lna} - \frac{P_{ref}}{|G|^2} \right) \tag{25}$$

$$P_{CAL} = \frac{P_{CAL0} - P_{CAL1}}{2} = |g|^2 |G|^2 G_1 G_2^* \left(P_a + P_{cal} + P_{lna} - \frac{P_{ref}}{|G|^2} \right) \tag{26}$$

3.6. Receiver bandpass calibration

The system response to the calibration noise is derived by differencing Equations (25), (26),

$$P_{CAL} - P_{OBS} = |g|^2 |G|^2 G_1 G_2^* P_{cal} \tag{27}$$

Dividing the Equation (25) by the system response to the calibration noise, we derive the bandpass calibrated spectrum in temperature unit,

$$T_{meas} = \frac{P_{OBS}}{P_{CAL} - P_{OBS}} \times T_{cal} = T_a + T_{lna} - \frac{T_{ref}}{|G|^2} \tag{28}$$

4. Measurement equation for real system

In real system performance, the three key assumptions of an ideal system do not hold true.

- The RF components have input-output impedances that are not perfectly matched with each other or with 50 Ohm transmission lines and result in multipath propagation effects within the system.
- The power splitter deviates from its ideal behaviour in two ways. 1. Due to amplitude imbalances, i.e., $|g_{\Sigma 1}|^2 \neq |g_{\Sigma 2}|^2$ and $|g_{\Delta 1}|^2 \neq |g_{\Delta 2}|^2$. and 2. The phase imbalances ($\angle g_{\Sigma 1} - \angle g_{\Sigma 2}$), ($\angle g_{\Delta 1} - \angle g_{\Delta 2}$) can deviate from their ideal values of 0° , 180° . This is analogous to additional electrical path length along one receiver channel with respect to the other.
- The receiver noise can also travel upward, opposite to the direction of propagation of the antenna noise.

In this section, we discuss the effects of such non-ideal behaviour on antenna, receiver, reference and calibration noise and show how they change our ideal measurement equation. Our calibration plane is at the output of the directional coupler, i.e., at the input of the LNA. Therefore, all noises are referred to at this point. The farther downstream is a point of impedance mismatch with respect to the calibration plane, the less significant is the reflected signal amplitude from that point of mismatch. From this perspective, impedance mismatch only at the calibration plane is of importance.

4.1. Real system response to Antenna noise

- **Effect of directional coupler on antenna noise:** A directional coupler can imprint spurious spectral response on the antenna noise within the observing band in two ways. 1. Due to impedance mismatch between the transmission line connecting the antenna output to port P_2 of the directional coupler, only a fraction, $(1 + \Gamma_D)$ fraction is transmitted to the directional coupler output where Γ_D is the voltage reflection coefficient at port P_2 . Γ_D fraction of the antenna voltage v_a is reflected back from port P_2 to the antenna as shown in Figure 6. The antenna reradiates

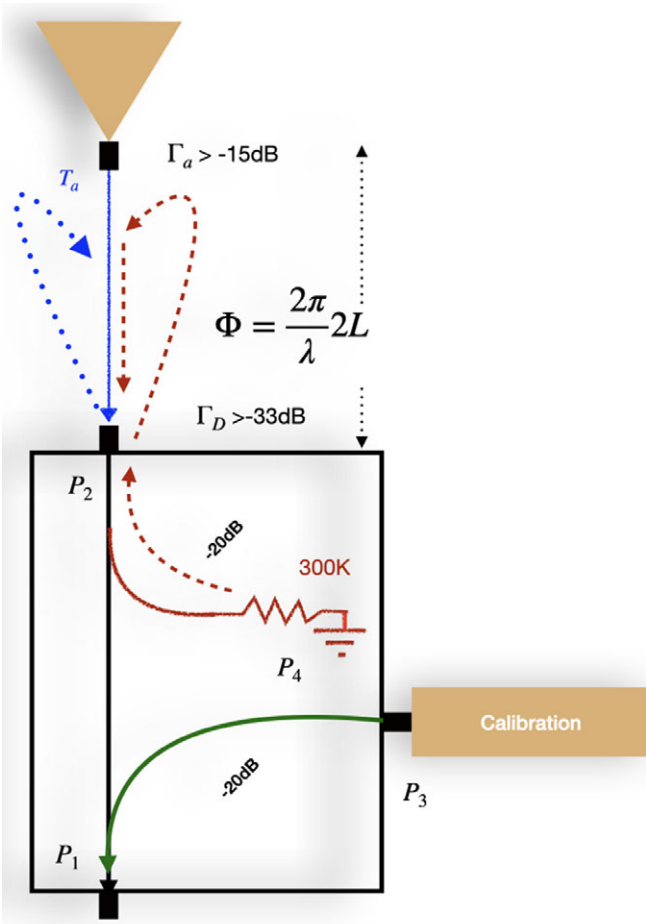


Figure 6. Schematic diagram of a unidirectional coupler with the fourth port P_4 internally terminated. Noise generated by the 50 Ohm termination at P_4 is coupled to the antenna path via port P_2 .

the majority of this reflected signal, and a small fraction Γ_a (antenna voltage reflection coefficient) is coupled back into the antenna path with a frequency-dependent phase delay $\Phi_1 = \frac{2\pi i2L}{\lambda}$ where L is the electrical path length between P_2 and the antenna output. The net antenna voltage at the output of the directional coupler after one reflection at the input of the directional coupler,

$$v'_a = v_a(1 + \Gamma_D)(1 + \Gamma_D\Gamma_a e^{i\Phi_1}) \quad (29)$$

2. A unidirectional coupler is a four-port device with the fourth port P_4 terminated internally by a 50 Ohm resistance that generates broadband noise at ambient temperature. Isolation between P_2, P_4 is 20 dB. For an ambient temperature of 300 K, a broadband noise of temperature 3 K is coupled to port P_2 that travels upward to the antenna. The antenna radiates the majority of this noise. Γ_a fraction of this noise is reflected back and added to the antenna signal path. Once again, at the $(1 + \Gamma_D)$ fraction of this noise voltage is transmitted by the directional coupler. The total noise voltage at the output of the directional coupler is,

$$v'_a = (1 + \Gamma_D) [v_a(1 + \Gamma_D\Gamma_a e^{i\Phi_1}) + v_{amb}\Gamma_{iso}\Gamma_a] \quad (30)$$

where, $\Gamma_{iso} = 10$ dB is the isolation between P_2, P_4 in voltage unit.

$$P'_a = |(1 + \Gamma_D)(1 + \Gamma_D\Gamma_a e^{i\Phi_1})|^2 P_a + |(1 + \Gamma_D)\Gamma_a\Gamma_{iso}|^2 P_{amb} \quad (31)$$

Since the calibration noise is injected at the output of the directional coupler, it only calibrates for any multiplicative path gain imprinted on v'_a from this point onwards. The spectral structures introduced by the directional coupler are preserved in the final bandpass calibrated data from which the Cosmic Dawn signal is expected to be detected.

- **Effect of stage1-LNA assembly on antenna noise:** The impedance mismatch between the directional coupler's output and the first LNA's input results in partial coupling of both v'_a and the calibration noise into the LNA. The rest is reflected back towards the antenna via the directional coupler. Γ_a fraction of this noise is coupled back into the system from the antenna terminal, and the rest is radiated. The net antenna voltage incident at the LNA input after one reflection from the LNA input and successive reflection from the antenna is,

$$v_{ain} = v'_a(1 + \Gamma_L)(1 + \Gamma_L\Gamma_a e^{i\Phi_2}) \quad (32)$$

where Γ_L is the voltage reflection co-efficient at the LNA input and $\Phi_2 = \frac{2\pi i2L}{\lambda}$ is the roundtrip phase delay. The output voltage of the LNA is,

$$v_{aout} = v'_a(1 + \Gamma_L)G(1 + \Gamma_L\Gamma_a e^{i\Phi_2}) = v'_aG(1 + \Gamma_L\Gamma_a e^{i\Phi_2}) \quad (33)$$

Since the term $(1 + \Gamma_L)$, and the LNA gain G both are multiplicative frequency responses of the LNA, for notational simplicity, we absorb the two terms into one single frequency-dependent amplifier gain term G .

At system state OBS0, i.e., when the antenna is connected to the Σ port of the splitter, the antenna voltages at the input of the correlator are,

$$v_{a1} = g_{\Sigma 1} v_{aout} G_1 \quad (34)$$

$$v_{a2} = g_{\Sigma 2} v_{aout} G_2 \quad (35)$$

The cross-power at the output of the spectrometer due to antenna noise,

$$P_{oa} = v_{a1} v_{a2}^* = g_{\Sigma 1} g_{\Sigma 2}^* G_1 G_2^* |v_{aout}|^2 = g_{\Sigma 1} g_{\Sigma 2}^* |G|^2 G_1 G_2^* |(1 + \Gamma_L\Gamma_a e^{i\Phi_2})|^2 P'_a \quad (36)$$

Similarly, at system state OBS1, i.e., when the antenna is connected to the Δ port of the splitter, the cross-power at the output of the spectrometer due to antenna noise,

$$P_{1a} = -g_{\Delta 1} g_{\Delta 2}^* |G|^2 G_1 G_2^* |(1 + \Gamma_L\Gamma_a e^{i\Phi_2})|^2 P'_a \quad (37)$$

4.2. Real system response to Receiver noise

Ideally, noise from the LNA has a downstream component, as discussed in Section 3.2. However, in real systems, it has a second component, correlated with the first, that travels opposite to the signal flow direction towards the antenna. After reaching the antenna, it is partially radiated, and the rest is reflected by the

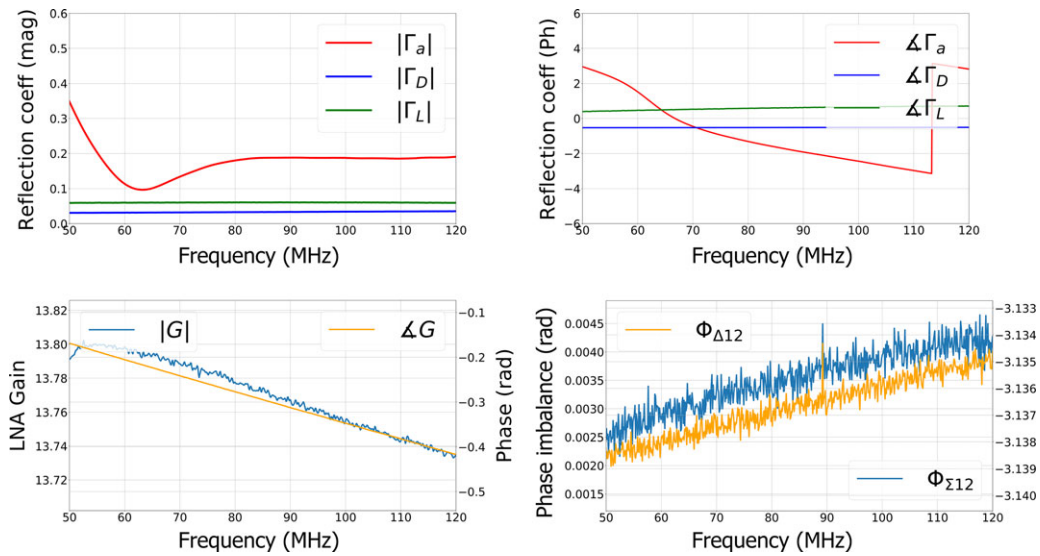


Figure 7. Electrical parameters of RF components that contribute to system response. Measurements of the magnitudes (top left) and phases (top right) of the voltage reflection coefficients at the antenna input (Γ_a), the LNA input (Γ_L) and the directional coupler input (Γ_D). Measurements of the magnitude and phase (bottom left) of the LNA complex gain. Phase imbalances of the power splitter path gains between Σ , port 1,2 and Δ , port 1,2, respectively. These system parameters collectively determine the spectral shapes of C_{sky} , C_{lms} , C_{ref} .

antenna and propagates downstream. We denoted the LNA noise voltage referred to its input as v_{lna} . If a fraction α of the total receiver noise travels upward, the total receiver noise incident at the input of the receiver in OBS0 state,

$$v_{rec1} = g_{\Sigma 1} v_{lna} G(1 + \Gamma_L) G_1(1 + \alpha \Gamma_L \Gamma_a e^{i\Phi_2}) \quad (38)$$

$$v_{rec2} = g_{\Sigma 2} v_{lna} G(1 + \Gamma_L) G_2(1 + \alpha \Gamma_L \Gamma_a e^{i\Phi_2}) \quad (39)$$

The cross-power at the output of the spectrometer due to receiver noise,

$$P_{or} = v_{rec1} v_{rec2}^* = g_{\Sigma 1} g_{\Sigma 2} |G|^2 G_1 G_2^* |(1 + \alpha \Gamma_L \Gamma_a e^{i\Phi_2})|^2 P_{lna} \quad (40)$$

Once again, we combine the term $(1 + \Gamma_L)$, and the LNA gain G for notational simplicity into one frequency-dependent amplifier gain term G .

In system state OBS1, the LNA1 is connected to the Δ port of the splitter. Receiver voltages at the input of the correlator are,

The cross-power at the output of the spectrometer due to receiver noise,

$$P_{1r} = v_{rec1} v_{rec2}^* = -g_{\Delta 1} g_{\Delta 2} |G|^2 G_1 G_2^* |(1 + \alpha \Gamma_L \Gamma_a e^{i\Phi_2})|^2 P_{lna} \quad (41)$$

Notable here is that the LNAs connected to the output of the power splitter also have upward travelling components that can travel to the antenna. However, the stage 1 LNA (ZFL-500HLN)-attenuator assembly offers a 50 dB reverse isolation to these upward propagating noises (25 dB in voltage) (ref: figure ZFL-500HLN reverse isolation). The antenna attenuates them by another 15 dB. The reflected noises once again go through the stage1 LNA (ZFL-500HLN)-attenuator assembly, which now offers a 10 dB attenuation and a 22 dB forward gain. Therefore, the part of these noise voltages that propagate downstream after being

reflected by the antenna has a total power attenuation of 53 dB or voltage attenuation of 27.5 dB. A typical value of α is 0.1. For ZFL-500LN, with a noise temperature of 275 K, a 27 K noise travels upward. After a 53 dB attenuation, only 0.0001 K noise is added to the downward travelling receiver noise. Even if a $\alpha = 1$, this contribution becomes 0.001 K. This is why we ignore the effects of the upward travelling component of the receiver noise from the LNAs to which the power splitter is connected.

4.3. Real system response to Reference noise

Power Splitter: In addition to the difference in path gain, the power splitter may have phase imbalances $\Phi_{\Sigma 12} = (\angle g_{\Sigma 1} - \angle g_{\Sigma 2})$, ($\Phi_{\Delta 12} = \angle g_{\Delta 1} - \angle g_{\Delta 2}$) can deviate from their ideal values of 0° , 180° . This is analogous to additional electrical path length along one receiver channel with respect to the other. The calibration noise calibrates the effect of the power splitter phase imbalance on the antenna noise since they are connected at the same port of the power splitter in both switch positions. Its effect on the reference noise remains uncalibrated. Our measurements show $\Phi_{\Sigma 12} = \Phi_{\Delta 12}$ (Figure 7) If $\Phi_{\Sigma 12} = \Phi_{\Delta 12} = \Delta\phi$ indicates the deviations from the ideal phase imbalances of 0° and 180° , then, when the reference is connected to the Δ port of the splitter, voltages at the input of the correlator are,

$$v'_{ref1} = g_{\Delta 1} v_{ref} G_1 \quad (42)$$

$$v'_{ref2} = -g_{\Delta 2} v_{ref} G_2 e^{i\Delta\Phi} \quad (43)$$

The cross-power at the output of the spectrometer due to reference noise,

$$P_{oref} = v'_{ref1} v_{ref2}^* = -g_{\Delta 1} g_{\Delta 2}^* G_1 G_2^* P_{ref} e^{-i\Delta\Phi} \quad (44)$$

and,

$$\begin{aligned}
 P_{1ref} &= v_{ref1} v_{ref2}^* \\
 &= g_{\Sigma 1} g_{\Sigma 2}^* G_1 G_2^* P_{ref} e^{-i\Delta\Phi}
 \end{aligned}
 \tag{45}$$

4.4. Real system response to total noise

$$\begin{aligned}
 P_{OBS0} &= P_{oa} + P_{or} + P_{oref} + P_{cor} \\
 &= g_{\Sigma 1} g_{\Sigma 2}^* |G|^2 G_1 G_2^* |(1 + \Gamma_L \Gamma_a e^{i\Phi_2})|^2 P_a' \\
 &\quad + g_{\Sigma 1} g_{\Sigma 2}^* |G|^2 G_1 G_2^* |(1 + \alpha \Gamma_L \Gamma_a e^{i\Phi_2})|^2 P_{lna} \\
 &\quad - g_{\Delta 1} g_{\Delta 2}^* G_1 G_2^* P_{ref} e^{-i\Delta\Phi} + P_{cor}
 \end{aligned}
 \tag{46}$$

Since the calibration noise is injected into the antenna path at the output of the directional coupler, when the calibration noise is ‘on’, the total cross-power output in state CAL0 is,

$$\begin{aligned}
 P_{CAL0} &= P_{oa} + P_{or} + P_{oref} + P_{cor} \\
 &= g_{\Sigma 1} g_{\Sigma 2}^* |G|^2 G_1 G_2^* |(1 + \Gamma_L \Gamma_a e^{i\Phi_2})|^2 (P_a' + P_{cal}) \\
 &\quad + g_{\Sigma 1} g_{\Sigma 2}^* |G|^2 G_1 G_2^* |(1 + \alpha \Gamma_L \Gamma_a e^{i\Phi_2})|^2 P_{lna} \\
 &\quad - g_{\Delta 1} g_{\Delta 2}^* G_1 G_2^* P_{ref} e^{-i\Delta\Phi} + P_{cor}
 \end{aligned}
 \tag{47}$$

Similarly, when the antenna and the reference positions are switched, the total complex cross-power spectrum measured in OBS1, CAL1 state are,

$$\begin{aligned}
 P_{OBS1} &= -g_{\Delta 1} g_{\Delta 2}^* |G|^2 G_1 G_2^* |(1 + \Gamma_L \Gamma_a e^{i\Phi_2})|^2 P_a' \\
 &\quad - g_{\Delta 1} g_{\Delta 2}^* |G|^2 G_1 G_2^* |(1 + \alpha \Gamma_L \Gamma_a e^{i\Phi_2})|^2 P_{lna} \\
 &\quad + g_{\Sigma 1} g_{\Sigma 2}^* G_1 G_2^* P_{ref} e^{-i\Delta\Phi} + P_{cor}
 \end{aligned}
 \tag{48}$$

Since the calibration noise is injected into the antenna path at the output of the directional coupler, when the calibration noise is ‘on’, the total cross-power output in state CAL1 is,

$$\begin{aligned}
 P_{CAL1} &= -g_{\Delta 1} g_{\Delta 2}^* G G_1 G_2^* |(1 + \Gamma_L \Gamma_a e^{i\Phi_2})|^2 (P_a' + P_{cal}) \\
 &\quad - g_{\Delta 1} g_{\Delta 2}^* G G_1 G_2^* |(1 + \alpha \Gamma_L \Gamma_a e^{i\Phi_2})|^2 P_{lna} \\
 &\quad + g_{\Sigma 1} g_{\Sigma 2}^* G_1 G_2^* P_{ref} e^{-i\Delta\Phi} + P_{cor}
 \end{aligned}
 \tag{49}$$

$$\begin{aligned}
 P_{OBS} &= \frac{P_{OBS0} - P_{OBS1}}{2} \\
 &= (g_{\Sigma 1} g_{\Sigma 2}^* + g_{\Delta 1} g_{\Delta 2}^*) |G|^2 G_1 G_2^* \times \\
 &\quad [|(1 + \Gamma_L \Gamma_a e^{i\Phi_2})|^2 P_a' \\
 &\quad + |(1 + \alpha \Gamma_L \Gamma_a e^{i\Phi_2})|^2 P_{lna} - \frac{P_{ref}}{|G|^2} e^{-i\Delta\Phi}]
 \end{aligned}
 \tag{50}$$

$$\begin{aligned}
 P_{CAL} &= \frac{P_{CAL0} - P_{CAL1}}{2} \\
 &= (g_{\Sigma 1} g_{\Sigma 2}^* + g_{\Delta 1} g_{\Delta 2}^*) |G|^2 G_1 G_2^* \times \\
 &\quad [|(1 + \Gamma_L \Gamma_a e^{i\Phi_2})|^2 (P_a' + P_{cal}) \\
 &\quad + |(1 + \alpha \Gamma_L \Gamma_a e^{i\Phi_2})|^2 P_{lna} - \frac{P_{ref}}{|G|^2} e^{-i\Delta\Phi}]
 \end{aligned}
 \tag{51}$$

Therefore, for real system performance, Equation (28) modifies to,

$$\begin{aligned}
 T_{meas} &= \frac{P_{OBS}}{P_{CAL} - P_{OBS}} \times T_{cal} = T_a' \\
 &\quad + \frac{|(1 + \alpha \Gamma_L \Gamma_a e^{i\Phi_2})|^2}{|(1 + \Gamma_L \Gamma_a e^{i\Phi_2})|^2} T_{lna} \\
 &\quad - \frac{e^{-i\Delta\Phi}}{|G|^2 |(1 + \Gamma_L \Gamma_a e^{i\Phi_2})|^2} T_{ref}
 \end{aligned}
 \tag{52}$$

Using Equations (32), (52) can be written as,

$$\begin{aligned}
 T_{meas} &= |(1 + \Gamma_D)(1 + \Gamma_D \Gamma_a e^{i\Phi_1})|^2 T_a \\
 &\quad + |(1 + \Gamma_D) \Gamma_a \Gamma_{iso}|^2 T_{amb} \\
 &\quad + \frac{|(1 + \alpha \Gamma_L \Gamma_a e^{i\Phi_2})|^2}{|(1 + \Gamma_L \Gamma_a e^{i\Phi_2})|^2} T_{lna} \\
 &\quad - \frac{e^{-i\Delta\Phi}}{|G|^2 |(1 + \Gamma_L \Gamma_a e^{i\Phi_2})|^2} T_{ref}
 \end{aligned}
 \tag{53}$$

We note that $T_a = G_a T_{sky}$. Also, the directional coupler and the reference 50 Ohm load are at the same ambient temperature within the frontend module box. Therefore, $T_{amb} = T_{ref}$. We verify this by measuring the temperature of the directional coupler and the reference load over a period of 12 h of observation using a platinum thermometer. In addition, the physical distance between the input of the directional coupler and the input of the LNA is less than 0.05 m. Therefore $\Phi_1 \approx \Phi_2 = \Phi$. Therefore, (53) can be written as,

$$\begin{aligned}
 T_{meas} &= |(1 + \Gamma_D)(1 + \Gamma_D \Gamma_a e^{i\Phi})|^2 G_a T_{sky} \\
 &\quad + \frac{|(1 + \alpha \Gamma_L \Gamma_a e^{i\Phi})|^2}{|(1 + \Gamma_L \Gamma_a e^{i\Phi})|^2} T_{lna} \\
 &\quad + [|(1 + \Gamma_D) \Gamma_a \Gamma_{iso}|^2 - \frac{e^{-i\Delta\Phi}}{|G|^2 |(1 + \Gamma_L \Gamma_a e^{i\Phi})|^2}] T_{ref} \\
 &= C_{sky} T_{sky} + C_{lna} T_{lna} + C_{ref} T_{ref}
 \end{aligned}
 \tag{54}$$

Due to averaging the spectra measured in two switch positions, the magnitude of the gain imbalances along the paths of the power splitter is removed in the process of the bandpass calibration. However, phase imbalances result in complex cross-power spectra contributed by the reference noise. The term $\Delta\Phi$ makes the term C_{ref} complex. We use the RF power splitter AMT-2+ from the mini-circuit. Phase imbalances ($\angle g_{\Sigma 1} - \angle g_{\Sigma 2}$), and ($\angle g_{\Delta 1} - \angle g_{\Delta 2}$) are shown in Figure 7. Any spectral ripple created by the phase imbalances within the power splitter paths in the antenna noise spectrum gets fully calibrated by the calibration noise. Another notable observation here is the contribution of the first stage LNA. For an ideal amplifier, $\alpha = 0$. This will result in an uncalibrated system bandpass response of the form $\frac{1}{|(1 + \Gamma_L \Gamma_a e^{i\Phi})|^2}$ in the LNA noise contribution. However, if $\alpha = 1$, the LNA bandpass response is identical to that of the calibration noise and is completely calibrated. Commonly, in radio telescopes, the first stage of amplifiers is the low-noise amplifiers. However, LNAs have poor input impedance match and extremely poor reverse isolation compared to a regular power amplifier. Poor impedance match will increase the ripple amplitude of $e^{i\Phi}$ for both LNA and reference noise. Poor reverse isolation will result in contribution from any other source of noise downstream, such as the LNA1,2 that can

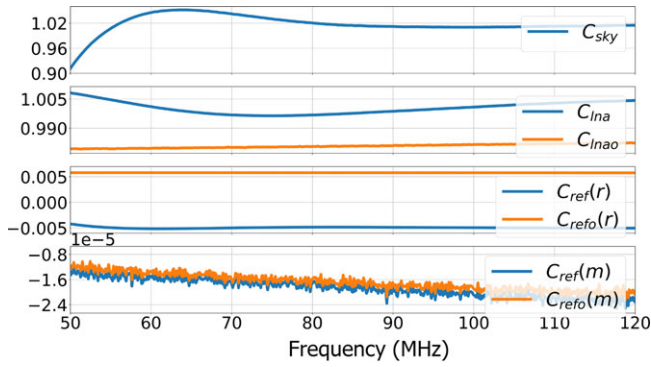


Figure 8. The residual uncalibrated bandpass responses C_{sky} , C_{Ina} , C_{ref} computed using the measurements of the RF components. Blue lines show the responses when the antenna is connected to the system input. The orange lines show the responses when the antenna input is connected to an open load. In this case, both the upward travelling receiver noise and the reference noise are entirely reflected back into the system with a roundtrip phase delay. $C_{sky} = 0$ as $G_a = 0$ when the antenna input is open. $C_{ref}(r)$ and $C_{ref}(m)$ are the real and the imaginary parts of the C_{ref} .

propagate upstream and create a spectral ripple. Therefore, for the purpose of this experiment, we chose the amplifier with a higher noise figure but better input impedance match and higher reverse isolation compared to conventional LNAs as the first stage of the amplifier. ZFL-500HLN has a noise figure of 3.8 dB, i.e., a noise temperature of $405\text{ K} \ll T_{sky}$ at all frequencies. The input return loss of the amplifier is $> 22.8\text{ dB}$, and the reverse isolation is 39 dB across the band of interest.

We measure input voltage reflection coefficient of the antenna (Γ_a) (Figure 7), the directional coupler (Γ_D) and the LNA (Γ_L) shown in the top left panel of Figure 6. We also measure the magnitude and phases of the complex voltage gains of the LNA as well as the phase imbalances $\Phi_{\Sigma 12}$ and $\Phi_{\Delta 12}$ between the paths of the power splitter. C_{sky} , C_{Ina} , C_{ref} computed from these measurements are shown in Figure 8. Given the spectral characteristics of C_{Ina} , C_{ref} , we assess the detectability of the reported absorption profile in Section 6.

The remaining system bandpass parameter C_{sky} represents the combined frequency response of the antenna and any external chromatic effects, such as the multipath propagation of the sky noise in the surroundings that remain uncalibrated. Antenna frequency response G_a is composed of two different effects. 1. Variation of the angular beam size with the frequency results in receiving the sky power from different areas of the sky at different frequencies. 2. Efficiency with which the antenna couples the sky power into the system—represented by the factor $(1 - |\Gamma_a|^2)$ that represents how much of the received power is actually coupled to the receiver. $|\Gamma_a|^2$ represents the return loss of power at the antenna terminal. In reality, when an antenna is placed over the ground and $|\Gamma_a|^2$ is measured, the measurement also includes any multipath propagation effects, including ground reflections and reflections from the immediate surroundings. For a wide-band antenna with a beam that covers roughly 30% of the sky at any time, there is no calibrator source in the sky comparable to the beam that can increase the system temperature significantly and give a “Cal-on” measurement like a point source calibration. Therefore, it is impossible to be able to measure or calibrate the beam-integrated frequency response due to the absence of any calibrator source in the far field. However, measurement of the antenna return loss can be used to assess the capacity of the antenna for this detection.

5. HYPEREION data

Output spectra of the HYPEREION system in various states are shown in Figure 9. The antenna input is terminated with a precision 50 Ohm broadband load at ambient temperature. In this case, $P_a = P_{50}$. The two columns show the real and the imaginary of the cross-power spectra. Four consecutive rows show the spectra recorded in four states (0,0); (0,1);(1,0);(1,1) of the system— P_{OBS0} , P_{CAL0} , P_{OBS1} , P_{CAL1} . The real and the imaginary part of the cross-power spectrum are of opposite signs in each system state. In switch position ‘0’, P_a , P_{Ina} are connected to the Σ port of the splitter and P_{ref} is connected to the Δ port. P_a and P_{ref} both are at ambient temperature, $P_a + P_{Ina} > P_{ref}$. Therefore, the real part of the cross-power spectrum is positive. However, the imaginary part of the cross-power spectrum is contributed by P_{ref} alone and, therefore, negative (Equation (54)).

5.1. Bandpass calibration

Averaging the ‘OBS’ and ‘CAL’ spectra in two switch positions results in P_{OBS} , P_{CAL} as defined by (50), (51). The system’s response to the calibration noise is derived by subtracting (50) from (51). The bandpass calibrated spectrum of the 50 Ohm termination is computed as $P_{meas}(50\text{ Ohm}) = \frac{P_{OBS}}{P_{CAL} - P_{OBS}}$. For each set of 4 spectra measured in 4 states of the system, we obtain one bandpass calibrated spectrum P_{meas} .

5.2. Absolute temperature calibration

Bandpass calibrated spectrum is to be multiplied by the system calibration temperature T_{cal} to obtain the spectrum in the temperature unit. To determine T_{cal} , we measure the spectrum of the precision 50 Ohm termination keeping it at different physical temperatures. A platinum resistance thermometer monitors the physical temperatures of both input 50 Ohm and the reference 50 Ohm. Physical temperatures are also the noise temperatures of the 50 Ohms since they are ‘matched’ to the system. The matched termination is first immersed in ice as a ‘cold’ load corresponding to a physical temperature of T_{cold} and then in ‘hot’ water as a ‘hot’ load corresponding to a physical temperature of T_{hot} . From these measurements, the system calibration temperature T_{cal} is given by

$$T_{cal} = \frac{T_{hot} - T_{cold}}{P_{50hot} - P_{50cold}} \quad (55)$$

We multiply the $P_{meas}(50)$ by T_{cal} we obtain bandpass calibrated spectrum in temperature unit as shown in Figure 10.

6. Data quality assessment

Based on our analytical modelling of the real system performance, we now assess if the system poses any limitation to detecting the absorption profile of the form (1). So far, no standardised formalism has been established to assess the data quality of any global 21 cm instruments to verify if a specific cosmological model of a Global 21 cm signal is detectable given the instrument performance. A commonly adopted approach is to model the system’s chromaticity by polynomials of various order (Singh et al. 2018; Bowman et al. 2018; Monsalve et al. 2017). However, this method is governed by the accuracy of our prior knowledge of the system’s chromaticity. While one can study constituent RF components of a system by simulation and bench-top testing when the end-to-end integrated system responds to the electromagnetic environment of the observing site. For such an assessment, one has to show that

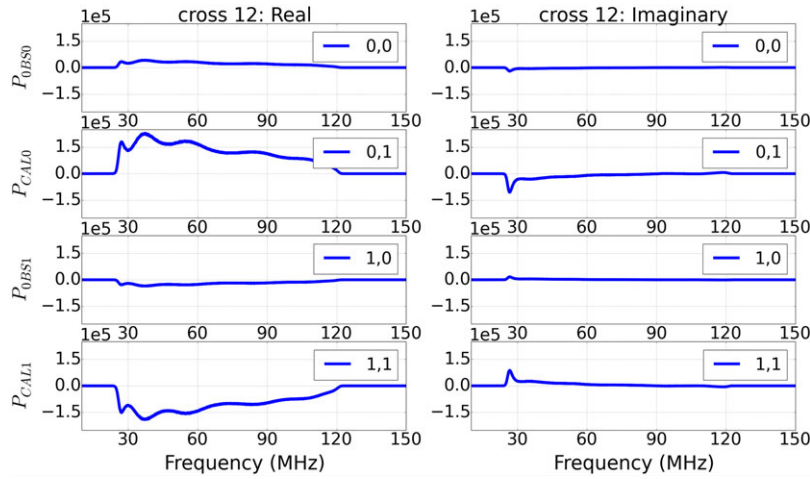


Figure 9. Raw spectra measured in four states of the system. Left and right column shows the real and the imaginary part of the measured cross-power.

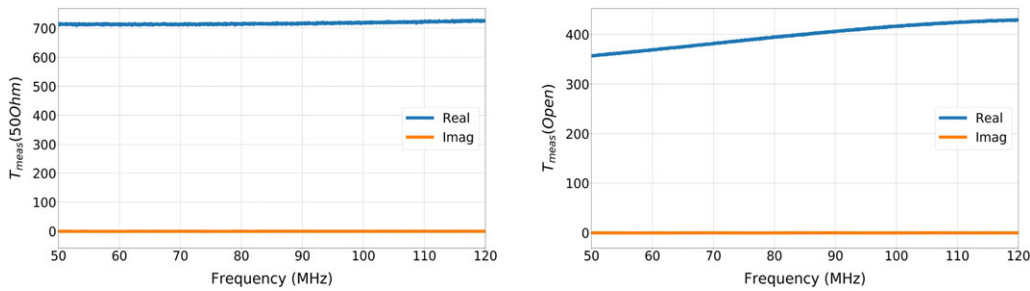


Figure 10. Bandpass calibrated spectrum in absolute temperature unit. Left: Antenna input terminated with a 50 Ohm load. Right: Antenna input terminated with a Open load.

residual uncalibrated system response does not inherently possess any spectral shape that can be confused with the intended signal. In the following section, we lay out a formalism to demonstrate that the uncalibrated system response that remains in our bandpass calibrated absolute temperature spectrum does not inhibit the detection of the Global 21 cm signal of the form (1). We explain this formalism with two examples.

6.1. Antenna input terminated with a 50 Ohm

In this case, in Equation (54), $\Gamma_a \approx 0$ and $T_{sky} = T_{amb} = T_{ref}$. $C_{sky} = |(1 + \Gamma_D)|^2$, $C_{lna} = 1$, $C_{ref} = \frac{e^{-i\Delta\Phi}}{|G|^2}$

$$T_{meas} = C_{sky}T_{sky} + C_{lna}T_{lna} + C_{ref}T_{ref}$$

$$= |(1 + \Gamma_D)|^2 T_{amb} + T_{lna} - \frac{e^{-i\Delta\Phi}}{|G|^2} T_{amb} \quad (56)$$

Since $\Gamma_a \approx 0$, the contribution from the isolated port of the directional coupler is negligible. Instead, the real part of the measured spectra is contributed by the thermal noise from the 50 Ohm input termination at ambient temperature, noise from the first LNA and the reference 50 Ohm thermal load. Since $\Gamma_a \approx 0$ noise from the terminated port of the directional coupler does not contribute to this T_{meas} . We refer to the total noise from the first LNA and the reference thermal load as the ‘receiver noise’ from hereon. The S_{11} of the termination is at the level of -48 dB. Any

upward travelling receiver noise will return with a 48 dB attenuation. A receiver noise of $T_{lna} = 400$ K will result in a reflected signal amplitude of <6 mK. Therefore, receiver reflection from the antenna input can be neglected in this configuration. The reference noise temperature $T_{ref} = 300$ K referred to the input of the first LNA is ≈ 2 K. The imaginary part of T_{meas} is contributed by the reference noise alone. For a 300 K ambient temperature and a 400 K receiver noise, $T_{meas} \approx 700$ K. Since the reference and the input noises are thermal, any additional spectral shape in this measurement is inherently attributed to the intrinsic noise from the LNA.

6.2. Antenna input terminated with an open load

In the next step, we replace the 50 Ohm termination at the input of the antenna with an open load. Any upward travelling receiver noise will be fully reflected from the antenna input, i.e., $\Gamma_a = 1$. In this case, in Equation (54), $\Gamma_a \approx 1$ and $T_{sky} = 0$. $T_{iso} = T_{ref}$

$$T_{meas} = \frac{|(1 + \alpha\Gamma_L e^{i\Phi})|^2}{|(1 + \Gamma_L e^{i\Phi})|^2} T_{lna}$$

$$+ [|(1 + \Gamma_D)\Gamma_{iso}|^2 - \frac{e^{-i\Delta\Phi}}{|G|^2|(1 + \Gamma_L e^{i\Phi})|^2}] T_{ref} \quad (57)$$

The real part of the bandpass calibrated spectrum is contributed by the receiver and reference noise, whereas the imaginary part

is contributed by the reference noise alone. Once again, since the reference is a thermal noise, any additional spectral shape in this measurement is inherently attributed to the intrinsic noise from the LNA.

6.3. Principal Component Analysis

Principal Component Analysis (PCA) is a method to find the fundamental ‘shapes’ present in a dataset without prior assumptions of their exact form. Principal Components are the orthogonal basis vectors that describe a dataset. Unlike describing a data set of multiple variables with chosen functional forms such as power law or polynomials, PCA first computes and characterises the variability in the data. A comprehensive description of PCA can be found in Jolliffe & Cadima (2016)

We consider each channel power $T_{meas}(v)$ as one variable in this work. The sample variance of $T_{meas}(v_i)$ at each channel ‘ i ’ is described by the radiometer equation and is determined by the system noise. Ideally, each channel measurement is independent of the other. Co-variability of measured T_{meas} between v_i, v_j shows the underlying spectral shape. Intrinsically, the covariance between two channels is contributed by T_{sky} . However, system-generated chromaticity, for example, quantities like $C_{sky}, C_{lms}, C_{ref}$ generate additional co-variability between a pair of channels. We detect these variabilities in the T_{meas} to assess the spectral shapes contributed by the system.

We take a set of ‘ p ’ number bandpass calibrated spectra ($p = 200$) $T_{meas}(v, t)$, measured at ‘ n ’ frequencies ($n = 4096$) and compute the covariance of power between any two frequencies. $T_{meas}(v, t)$ is a data set of $p \times n$ dimensional vectors, i.e., a $p \times n$ matrix. We drop the variable ‘ t ’ in this spectral shape analysis for notational simplicity. Each $T_{meas}(v_i)$ is a random variable that represents the measured power at the i ’th frequency channel. A spectral shape in the measured data means $T_{meas}(v_i)$ is covariant with $T_{meas}(v_j)$ in a certain way for all ‘ i, j ’. There can be multiple orthogonal spectral shapes resulting in multiple covariances. We compute the covariance matrix of $T_{meas}(v)$ by,

$$C_{ij} = \frac{\sum_p T_{meas}(v_i) \cdot T_{meas}(v_j)}{(p - 1)} \tag{58}$$

where p is the number of measurements of T_{meas} .

Note on mean subtraction: The covariance method is used to find how a pair of random variables vary with each other. These variables can have different scales and units of measurement. So, they are standardised prior to computing the covariances, i.e., their mean is subtracted from all sample values, and their variances weigh each sample. This ensures the computed covariance between a pair of variables is not dominated by the variable with a higher variance. When there is no correlation between two variables, their covariance reveals ‘shape/pattern/trend’ in their relationship. Standardisation is important while comparing variability trends between two variables with different units of measurement and measurement errors. In that case, the covariance matrix is defined as,

$$C_{ij} = \frac{\sum_p [T_{meas}(v_i) - \mu_i] \cdot [T_{meas}(v_j) - \mu_j]}{(p - 1)} \tag{59}$$

Where μ_i is the sample mean of $T_{meas}(v_i)$.

However, when we compare two deterministic variables that are highly correlated with the same unit of measurement and variances, there is information in the differences between their means

and variances. Standardisation will destroy this information content. PCA on non-standardised data is done in specific cases. A discussion on this can be found in Kriegsman (2016). Another discussion on when not to use standardisation can be found in STAT505 (2022).

In our case, T_{meas} at all channels has the same unit of power. We investigate how the measured power co-vary systematically between a pair of channels. When a matched load terminates the input at ambient temperature, each channel has the same mean power given by the ambient temperature, and there are no internal reflections from the antenna input. They also have identical measurement errors (determined by the radiometer equation). So, the data are automatically standardised.

When an open load terminates the input, complete reflection of the upward travelling receiver noise creates a spectral ripple. It changes the mean power at each channel by a few tens of Kelvin. The mean power at every frequency (sample mean)—vs—frequency is a shape present in the data. In this case, it is a measure of the system’s internal reflection. Subtracting the sample mean of every channel from each spectrum will destroy this information. When data is not standardised, this shape will be described by one or more Principal Components. Similarly, differences between variances of channel power are also an indicator of additional spectral shapes. Upon complete reflection from the antenna input, the upward travelling receiver noise is added to the downstream signal path. This changes the channel variances. Increased variances show which channels are more affected due to internal reflection and contribute to additional spectral patterns beyond what is described by the mean. Standardisation of channel power will force them to have unit variance and destroy some spectral structures.

Therefore, we do not subtract a sample mean from the data in our analysis to standardise it. Instead, we use the python routine ‘numpy.cov’ that computes a constant mean from the entire dataset and subtracts this value from every measurement prior to computing the covariance matrix. In the absence of higher-order spectral shapes, this only reduces the Eigenvalue of the first Principal Component.

Figure 11 first panel shows the C_{ij} computed from a set of T_{meas} when the antenna input is terminated with a 50 Ohm and an open load. The covariance matrix of measured power is symmetric, i.e., $C_{ij} = C_{ji}$. The second panel shows the diagonal C_{ii} of the covariance matrices which is the variance of measured power at a given frequency. Per channel variance in the bandpass calibrated spectrum can also be calculated as follows. From the radiometer equation, per channel variance in measured $P_{OBS0}, P_{OBS1}, P_{CAL0}, P_{CAL1}$ are given by,

$$\sigma_{OBS0} = \sigma_{OBS1} = T_{sys}/(\Delta v \Delta \tau)^{1/2} \tag{60}$$

and,

$$\sigma_{CAL0} = \sigma_{CAL1} = T'_{sys}/(\Delta v \Delta \tau)^{1/2} \tag{61}$$

where, Δv is the channel bandwidth and, $\Delta \tau$ is the integration time in each state. Therefore, when averaged over two switched positions,

$$\sigma_{OBS} = (\sigma_{OBS0}^2 + \sigma_{OBS1}^2)^{1/2} = \sqrt{2} T_{sys}/(\Delta v \Delta \tau)^{1/2} \tag{62}$$

and mean channel power,

$$\mu_{OBS} = T_{sys} \tag{63}$$

$$\sigma_{CAL} = (\sigma_{CAL0}^2 + \sigma_{CAL1}^2)^{1/2} = \sqrt{2} T'_{sys}/(\Delta v \Delta \tau)^{1/2} \tag{64}$$

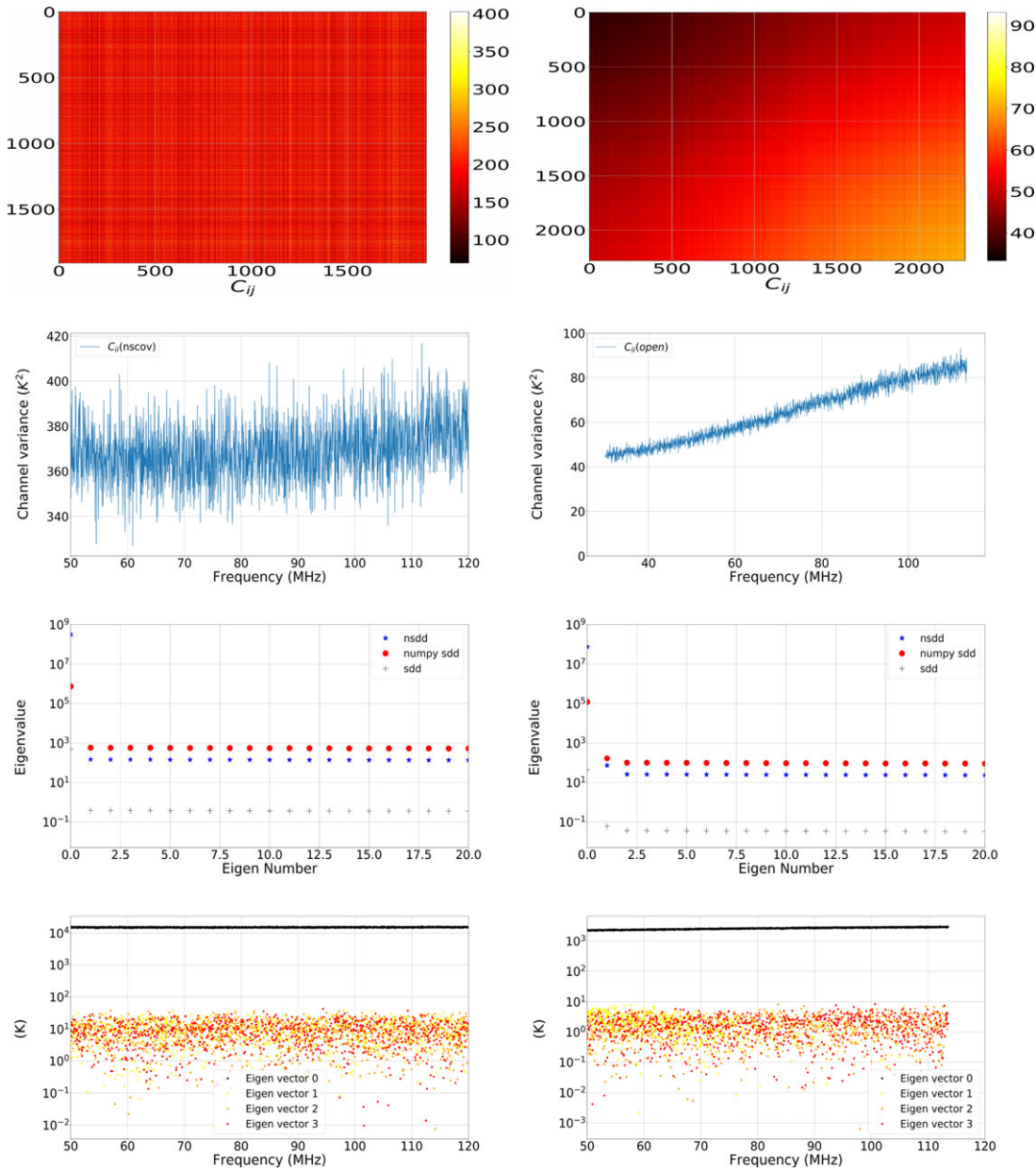


Figure 11. First row: The covariance matrices of $T_{meas}(50 \text{ Ohm})$ and $T_{meas}(Open)$ computed along the frequency axis. Since the input is thermal noise, the individual channel powers are uncorrelated. If the instantaneous channel power in the i 'th channel is high, it is reflected in all C_{ij} resulting in fine vertical lines. The occurrence of such a sample is randomly distributed across all frequencies resulting in fine vertical lines distributed across the frequencies. Second row: The diagonal element of covariance matrices, i.e., the variance of measured power at a given frequency channel. Third row: Eigenvalues of C_{ij} for different standardisations. 'nsdd' shows the Eigenvalues that are computed from the Covariance matrix without any standardisation of the data. 'NumPy sdd' shows the Eigenvalues when the covariance matrix is computed using 'numpy.cov' python routine as shown in the first row, first panel. In this case, a constant mean is subtracted from each measurement prior to computing the covariance matrix. The 'sdd' show the Eigen Values computed from the Covariance matrix when the data is fully 'standardised', i.e., a sample mean is subtracted from each measurement and weighted by the sample variance of that channel. This reduces the amplitude of all principal components. c Fourth row: Principal Components of $T_{meas}(50 \text{ Ohm})$ and $T_{meas}(Open)$ as functions of frequency.

Per channel variance in the calibration template $P_{CAL} - P_{OBS}$ is given by,

$$\sigma_{CAL-OBS} = (\sigma_{CAL}^2 + \sigma_{OBS}^2)^{1/2} = \sqrt{(2)[(T'_{sys} + T_{sys})/(\Delta V \Delta \tau)]^{1/2}} \quad (65)$$

and corresponding mean is,

$$\mu_{CAL-OBS} = (T'_{sys} - T_{sys}) \quad (66)$$

Each channel of the bandpass calibrated spectrum $Z = \frac{P_{OBS}}{(P_{CAL} - P_{OBS})} = \frac{X}{Y}$ is a ratio of two independent Gaussian random

variables. Its distribution is known as the ratio distribution, given by Díaz-Francés & Rubio (2012),

$$p_Z(z) = \frac{b(z) \cdot c(z)}{a^3(z)} \frac{1}{\sqrt{2\pi} \sigma_x \sigma_y} \left[2\Phi\left(\frac{b(z)}{a(z)}\right) - 1 \right] + \frac{1}{a^2(z) \cdot \pi \sigma_x \sigma_y} \exp\left[-\frac{1}{2} \left(\frac{\mu_x^2}{\sigma_x^2} + \frac{\mu_y^2}{\sigma_y^2}\right)\right] \quad (67)$$

where,

$$a(z) = \sqrt{\frac{1}{\sigma_x^2}(z)^2 + \frac{1}{\sigma_y^2}} \tag{68}$$

$$b(z) = \frac{\mu_x}{\sigma_x^2}z + \frac{\mu_y}{\sigma_y^2} \tag{69}$$

$$c(z) = \exp\left[\frac{1}{2} \frac{b^2(z)}{a^2(z)} - \frac{1}{2} \left(\frac{\mu_x^2}{\sigma_x^2} + \frac{\mu_y^2}{\sigma_y^2}\right)\right] \tag{70}$$

$$\Phi(z) = \int_{-\infty}^z \frac{1}{\sqrt{2\pi}} e^{-\frac{1}{2}u^2} du \tag{71}$$

If the mean and variance μ_x, μ_y and σ_x and σ_y of the variables X, Y are strictly positive, and the coefficient of variation, defined as $\delta_x = \sigma_x/\mu_x = 1/(\Delta T)$ and $\delta_y = \sigma_y/\mu_y 1/(\Delta T)$ are both less than unity, the distribution could be approximated as a normal distribution with mean $\mu_z = \mu_x/\mu_y$ and standard deviation $\sigma_z = (\mu_x/\mu_y)\sqrt{(\delta_x^2 + \delta_y^2)}$. These conditions hold true for our measurements.

When a thermal load is attached to the antenna, $\mu_{OBS} = T_{sys} \approx 700$ K. When a 3 dB ENR calibration noise is added to the system, $T'_{sys} \approx 2 * T_{sys}$ K. Therefore, $\mu_{CAL-OBS} \approx T_{sys}$ K. Using these values, when the input is terminated with a matched 50 Ohm load at 300 K temperature, accounting for the contribution from all sources of noise in P_{OBS} , per channel variance is expected to be of the order of ≈ 340 K. We obtain a slightly higher variance from the measurement, indicating the mean ambient and receiver temperature may be slightly higher than 300, 400 K.

Therefore, when no other system-induced spectral shape is present in the data, channel variances are expected to be Gaussian and of the same order as the covariance between two different channels. When antenna input is terminated with an open, the upward travelling receiver noise is reflected back into the system and added to the signal path downstream. This increases the mean power in each channel. In addition, the systematic increase in the increased variance of power per channel indicates that the reflected wave has an additional spectral shape. Thermal variance can be reduced by averaging multiple measurements of $T_{meas}(v, t)$ over time, whereas systematic spectral variances resulting from the spectral shape will not be averaged to zero.

We decompose the covariance matrix into Eigenvalues and Eigenvectors. Principal Components of $T_{meas}(v)$ are given by the eigenvectors of the covariance matrix, while the corresponding Eigenvalues give their strength. They are orthogonal basis vectors just like, for example, Fourier Components. The key difference is that, unlike the Fourier Transform, the particular mathematical form of the basis vector is not known a priori and is determined from the measured $T_{meas}(v)$ itself. Our goal is to demonstrate that HYPEREION’s chromaticity instrument does not contain a spectral response identical to the Cosmic Dawn signal detected by EDGES. The Eigenvalues have the same units as the elements of the covariance matrix, i.e., $Kelvin^2$. The first eigenvector of the covariance matrix is the first Principal Component (PC) of $T_{meas}(v)$. It represents the largest and the most dominant spectral shape across frequencies. The successive Principal Components represent the spectral shapes that are orthogonal to the first PC and are present in the data with lower magnitude. The third row shows the first 20 Eigenvalues of C_{ij} . Once again, in a perfect system, only one Principal Component is required for describing T_{meas} . C_{ij} of 50 Ohm shows there is only one Eigenvalue corresponding to the one Principal Component of variation in T_{meas} . All other Eigenvalues are four orders of magnitude lower than the first

at a noise level. For $T_{meas}(open)$, the spectral ripple introduced due to the complete reflection of the upward travelling receiver noise results in a prominent second Eigenvalue.

The fourth panel shows the Eigenvectors as a function of frequency weighted by the corresponding eigenvalues. Notable here is that $T_{meas}(50\text{ Ohm})$ spectra contain only one Principal Component that describes the smooth variation of the $T_{meas}(v)$ over frequency. Higher-order Principal Components are four orders of magnitude smaller than the ‘0’th Principal Component. $T_{meas}(Open)$ shows the first Principal Component similar to $T_{meas}(50\text{ Ohm})$. But the second Principal Component (yellow) is no longer noise-like and separates itself from higher-order Principal Components.

6.4. Interpretation

In an ideal system, in the absence of any internal reflections of the receiver and reference noise from the antenna terminal, $T_{meas}(50\text{ Ohm})$ should be described by a constant temperature across all frequencies if the receiver noise is also thermal. In the context of Principal Component Analysis, this implies two things. 1. In such a system, the covariance matrix of $T_{meas}(50\text{ Ohm})$ should have only one Eigenvalue of significance. 2. Corresponding Principal Component of $T_{meas}(50\text{ Ohm})$ is described by a constant, i.e., by a polynomial of order ‘0’. Figure 11, row 3, the first panel shows, indeed, the covariance matrix has one Eigenvalue of significance corresponding to one Principal Component. Figure 12 top panel shows $T_{meas}(50\text{ Ohm})$ when described by the first PC and with successive addition of up to 4th PC to the first PC. The bottom panel shows residual $T_{meas}(50\text{ Ohm})$ composed of all higher-order PCs. The successive addition of more PCs only reduces the spectral variance. Note: since we have $n = 4\ 096$ frequency channels, there are also 4 096 Principal Components. When we subtract the first and the most significant PC, the residual is composed of 4 095 PCs. When we successively subtract more PCs up to the 4th PC, the residual is composed of 4 094, 4 093, and 4 096 PCs, all of which are random noise. Since there is no information of significance in these PCs, their subtraction only changes the residual noise statistics marginally.

We compare the PCA with the polynomial modelling of T_{meas} . Figure 13 shows fits with orders of polynomials 0 to 4 and the fit residuals. Corresponding histograms are shown in Figure 14. The mean and the variance of the fit residuals remain unchanged when fitted with the polynomial order above 2. This is the minimum order of the polynomial required to describe the receiver noise spectrum in HYPEREION measurements. Notable here is that a polynomial of order 2 is also a maximally smooth function (MSF). Singh et al. (2021), Bevins et al. (2021) have demonstrated that to recover a Global 21 cm signal from a wideband radio background measurements, the residual system response in the measured data should be modelled as MSF, hardware implementation of which is the greatest challenge faced by experiments that are aiming to detect the global 21 cm signal by precision radio background measurement.

When the antenna input is terminated with an open load, complete reflection of the upward travelling system noise generates an additional Principal Component of significance. Figures 13, 14 show the measured spectra fitted with orders of polynomials 0–4, the fit residuals, and corresponding histograms. We overlay the EDGES’s Cosmic Dawn signal on top of the residual receiver noise after fitting the 3,4th order polynomial in the extreme case of total

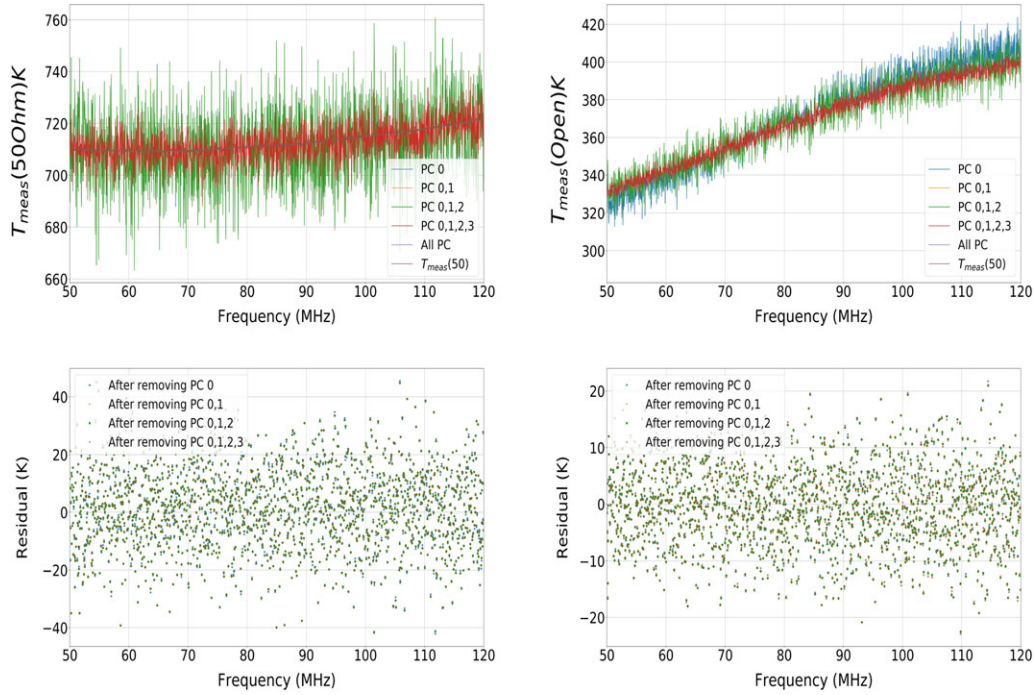


Figure 12. Top panel: Real parts of $T_{meas}(50\text{ Ohm})$, $T_{meas}(open)$ when described by the first PC and with successive addition of up to 4th PC to the first PC. Bottom panel: Residuals after projecting successively increasing number of Principal Components onto $T_{meas}(50\text{ Ohm})$, $T_{meas}(open)$.

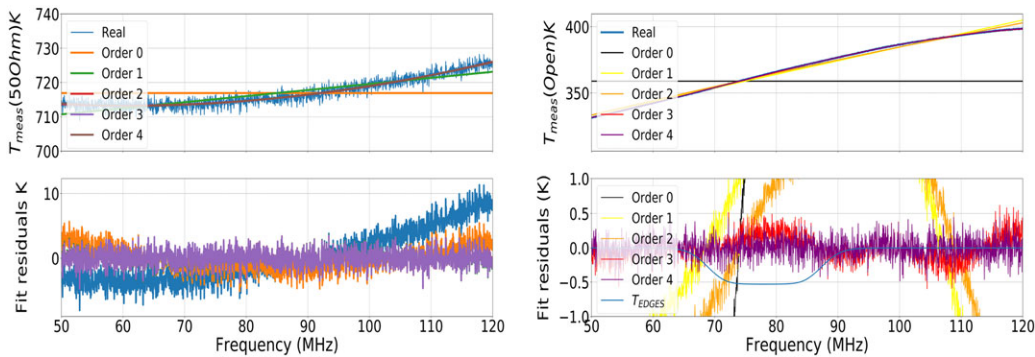


Figure 13. Top panel: Real parts of $T_{meas}(50\text{ Ohm})$, $T_{meas}(open)$ fitted with polynomials of order 0 to 4. Bottom panel: Residuals of the fit. For comparison, the EDGES Cosmic Dawn signal is overlaid with the residuals in the open case.

internal reflection of the receiver noise. Notable here is, in case of joint fitting of the sky spectrum and systematics, polynomials of order 3, 4 will also subsume a part of the Cosmic Dawn signal. This is illustrated and addressed in our foreground simulation work elsewhere. A 3rd-order polynomial is required to describe $T_{meas}(open)$. Fitting a polynomial of higher order doesn't improve the residuals. The presence of an additional Principal Component in $T_{meas}(open)$ requires higher-order polynomials to describe the measured data.

The 50 Ohm and an open load spectra describe the behaviour of HYPEREION system under two boundary conditions of 'no internal reflection' of receiver noise and 'complete internal reflection' of receiver noise. When HYPEREION antenna is connected, the system response will partially reflect the receiver noise from

the antenna terminal. Therefore, it will require a polynomial of order between 2–3 to describe the chromatic contribution of C_{Ina} , C_{ref} , T_{Ina} , T_{ref} in the measured data. This is the key difference between EDGES's instrument calibration and that of HYPEREION. In the EDGES's detection of the Cosmic Dawn signal, the measured spectra are calibrated for receiver noise using five receiver noise parameters that are predetermined from the laboratory measurements prior to observation by terminating the antenna input with open, short and 50 Ohm. Each of these parameters is then fitted with a 7th-order polynomial (Monsalve et al. 2017). These polynomials are then used to calibrate the final spectrum from which the Cosmic Dawn signal is estimated (Bowman et al. 2018). The Cosmic Dawn signal of the form detected by EDGES is described as a flattened Gaussian between 60–94 MHz.

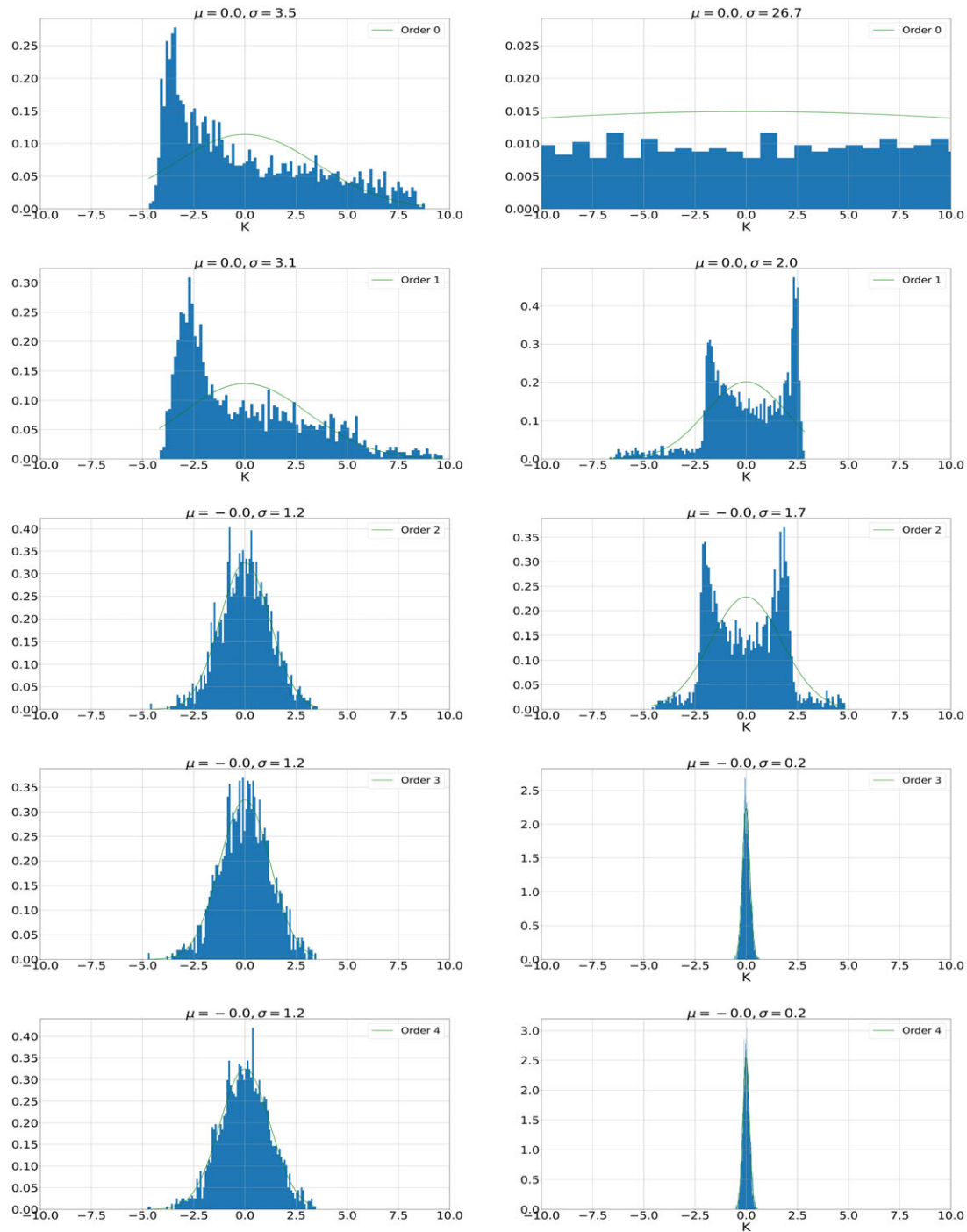


Figure 14. Histogram of the residuals after polynomials of 0–4 (top to bottom) are fitted to the real parts of $T_{\text{meas}}(50 \text{ Ohm})$ (left), $T_{\text{meas}}(\text{Open})$ (right). Units of the x-axis are in Kelvin.

The same can be described by a polynomial of order eight or higher, as shown in Figure 15.

Zheng et al. (2017), de Oliveira-Costa et al. (2008) have demonstrated that diffused Galactic radio emission, aka radio foreground that constitutes T_{sky} in equation 54, has three Principal Components of variation across the frequencies. They also showed that these Principal Components are best fitted with a polynomial of order 3 in log space. Bernardi, McQuinn, & Greenhill (2015),

Bowman et al. (2018) have also shown that polynomials of order 5, 6 improve the foreground residuals below a few 10s of m Kelvin. EDGES measurements require polynomials of order 5th or higher to describe the antenna gain, reflection coefficient and receiver calibration solutions (refer to ‘Extended Data Figure 4 Antenna beam model’, ‘Extended Data Figure 5 Calibration parameter solutions’, ‘Extended Data Figure 6 Raw and processed spectra’, in Bowman et al. (2018) and the references therein). This is higher

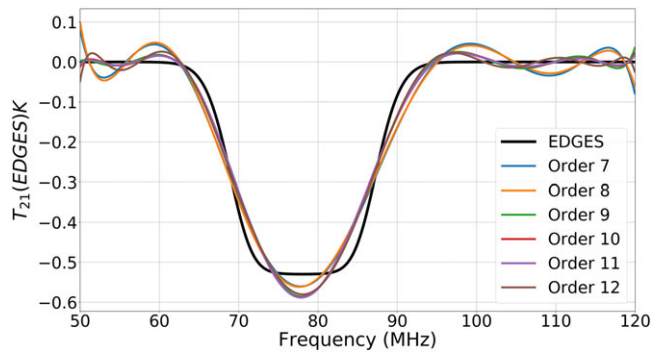


Figure 15. Cosmic Dawn signal detected by EDGES described by polynomial basis functions.

than what is needed to describe the sky signal indicating spectral variations in the data are dominated by receiver noise internal to the instrument. Receiver noise calibration by 7th-order polynomials will only leave higher-order variations in the calibrated data. This makes the presence of the signal in the background spectrum ambiguous.

The number of Principal Components required to describe the HYPEREION instrument response is smaller than the number of Principal Components required to describe the radio foreground. These Principal Components also overlap with that of the foreground and are accounted for in the process of foreground subtraction. In reality, HYPEREION receiver will be able to detect any form of the 21 cm Global signal that can be described by polynomials of order higher than what is needed to describe the foreground. When the antenna is connected to the spectrometer, the $T_{meas}(sky)$ will be dominated by the T_{sky} . In addition, C_{sky} will imprint its chromaticity on T_{meas} by modulating T_{sky} . C_{sky} can not be measured in situ or in the lab. It can be computed using electromagnetic simulation of G_a and Γ_a which is outside the scope of this paper and will be presented elsewhere. However, C_{sky} can be estimated from the measured data. Since the receiver and the foreground both can be described by only three Principal Components, any additional Principal Component in $T_{meas}(sky)$ will be generated by the C_{sky} . For a system like HYPEREION that is not limited by the receiver noise reflection inside or outside the system, the number of Principal Components generated by C_{sky} is the factor that determines whether or not the system can detect the Cosmic Dawn signal. The antenna performance of HYPEREION for determining C_{sky} will be discussed elsewhere.

7. Summary

In this paper, we presented the system design of a single-element radio telescope for precision measurement of the diffuse radio background between 50–120 MHz. System design is motivated by the need to characterise the system's non-ideal behaviour to the extent that ensures corroboration of the first reported detection of the Cosmic Dawn signal by EDGES. A power splitter preceded by a cross-over switch splits the antenna and the first stage LNA signal into two halves before feeding into two identical channels of a cross-correlation spectrometer. The calibration strategy eliminates any additive noise contribution post-switching stage and yields a differential measurement of antenna+receiver

noise temperature with respect to an internal reference termination at ambient temperature. The residual uncalibrated system response is composed of receiver and reference noise spectra that are modulated by impedance mismatches along the signal path from the antenna to the correlator. We present, in brief, a Principal Component Analysis formalism to quantify this residual system response in a model-independent way. We show that our selection of system components ensures that the residual uncalibrated system response is a Maximally Smooth Function. Spectral variability due to internal systematics is represented by a polynomial of the order less than the currently accepted description of foreground that of the foreground and, therefore, will be accounted for in the foreground modelling itself. These are the characteristics that distinguish HYPEREION from other contemporary instruments. Our system design and selection of RF components are motivated by some unconventional radio telescope design criteria, such as using the first stage amplifiers, not with the lowest noise figure but with better input-output impedance match in order to contain system response within the foreground Principal Components. As a MIL-STD-461 F qualified system with negligible emission, coupling of receiver noise back into the system after reflection from outside the antenna is also negligible. All these collectively ensure that the spectral variability due to the uncalibrated response of the system is well below that of the chromaticity of the sky signal T_{sky} in the measured data. Given its hardware design, observation and calibration strategy, and the performance of the HYPEREION receiver system, successful detection of the Cosmic Dawn signal by HYPEREION is reliant on antenna frequency response and external observing conditions such as the ground effect, multipath propagation effects and radio frequency environment of the observing site.

Acknowledgment. HYPEREION antenna is designed, developed, and built in the Radio Astronomy Laboratory at the University of California at Berkeley and was field tested at the Owen's Valley Radio Observatory in Big Pine, California. This work was funded by the CAREER grant of Dr. Aaron Parsons. The antenna system and associated hardware were transported to CIRA to be used for this work. We thank Dr. Aaron Parsons for this support.

Data Availability. System data will be made available on appropriate request.

References

- Barkana, R. 2018, *Natur*, 555, 71
- Barkana, R., Outmezguine, N. J., Redigol, D., & Volansky, T. 2018, *PhRvD*, 98, 103005
- Bernardi, G., McQuinn, M., & Greenhill, L. J. 2015, *ApJ*, 799, 90
- Bernardi, G., et al. 2016, *MNRAS*, 461, 2847
- Bevins, H. T. J., et al. 2021, *MNRAS*, 502, 4405
- Bowman, J. D., Rogers, A. E. E., Monsalve, R. A., Mozdzen, T. J., & Mahesh, N. 2018, *Natur*, 555, 67
- Burns, J., et al. 2021, arXiv e-prints, arXiv:2103.05085
- Burns, J. O., et al. 2017, *ApJ*, 844, 33
- Bye, C. 2021, in American Astronomical Society Meeting Abstracts, Vol. 53, American Astronomical Society Meeting Abstracts, 525.02
- Díaz-Francés, E., & Rubio, F. J. 2012. <https://link.springer.com/article/10.1007/s00362-012-0429-2>
- de Lera Acedo, E. 2019, in 2019 International Conference on Electromagnetics in Advanced Applications (ICEAA), 0626
- de Oliveira-Costa, A., et al. 2008, *MNRAS*, 388, 247
- Dilullo, C., Taylor, G. B., & Dowell, J. 2020, *JAI*, 9, 2050008
- Fialkov, A., Barkana, R., & Cohen, A. 2018, *PhRvL*, 121, 011101
- Furlanetto, S. R. 2006, *MNRAS*, 371, 867

- Furlanetto, S. R., Oh, S. P., & Briggs, F. H. 2006, *PhR*, 433, 181
- Hills, R., Kulkarni, G., Meerburg, P. D., & Puchwein, E. 2018, ArXiv e-prints, arXiv:1805.01421
- Jolliffe, I. T., & Cadima, J. 2016, *PTRSL*, 374, 20150202
- Kriegsman, M. 2016
- Mahesh, N., et al. 2021, *AJ*, 162, 38
- Monsalve, R. A., Rogers, A. E. E., Bowman, J. D., & Mozdzen, T. J. 2017, *ApJ*, 835, 49
- Morales, M. F., & Wyithe, J. S. B. 2010, *ARA&A*, 48, 127
- Mozdzen, T. J., Mahesh, N., Monsalve, R. A., Rogers, A. E. E., & Bowman, J. D. 2019, *MNRAS*, 483, 4411
- Nambissan T., J., et al. 2021, arXiv e-prints, arXiv:2104.01756
- Patra, N., Subrahmanyan, R., Raghunathan, A., & Udaya Shankar, N. 2013, *ExpAs*, 36, 319
- Patra, N., Subrahmanyan, R., Sethi, S., Udaya Shankar, N., & Raghunathan, A. 2015, *ApJ*, 801, 138
- Philip, L., et al. 2019, *JAI*, 8, 1950004
- Price, D. C., et al. 2018, *MNRAS*, 478, 4193
- Pritchard, J. R., & Loeb, A. 2012, *RPPh*, 75, 086901
- Raghunathan, A., Shankar, N. U., & Subrahmanyan, R. 2013, *IEEE TAP*, 61, 3411
- Rogers, A. E. E., & Bowman, J. D. 2008, *AJ*, 136, 641
- Shaver, P. A., Windhorst, R. A., Madau, P., & de Bruyn, A. G. 1999, *MNRAS*, 345, 380
- Sims, P. H., & Pober, J. C. 2020, *MNRAS*, 492, 22
- Singh, S., & Subrahmanyan, R. 2019, *ApJ*, 880, 26
- Singh, S., et al. 2018, *ExA*, 45, 269
- Singh, S., et al. 2021, arXiv e-prints, arXiv:2112.06778
- Sokolowski, M., et al. 2015, *PASA*, 32, e004
- STAT505. 2022, MS Windows NT Kernel Description
- Thekkeppattu, J. N., McKinley, B., Trott, C. M., Jones, J., & Ung, D. C. X. 2022, *PASA*, 39, e018
- Voytek, T. C., Natarajan, A., Jáuregui Garca, J. M., Peterson, J. B., & López-Cruz, O. 2014, *ApJ*, 782, L9
- Xiao, L., et al. 2019, *PhRvD*, 99, 023528
- Zheng, H., et al. 2017, *MNRAS*, 464, 3486